Experiments in Fluids (2026) 67:73
https://doi.org/10.1007/s00348-026-04221-2

RESEARCH ARTICLE

Unsteady aerodynamics of a plunging airfoil at large angles of attack

Guanqun Xu[1] · Andrea Sciacchitano[1] · Carlos Ferreira[1] · Wei Yu[1]

Received: 10 November 2025 / Revised: 24 March 2026 / Accepted: 30 March 2026

Abstract

During wind turbine installation or idling, the blades often operate at large angles of attack, where vortex-induced vibration (VIV) can occur. This study experimentally investigates the aerodynamic characteristics of a plunging NACA0021 airfoil at a fixed angle of attack of 90° and amplitude of one chord length, focusing on vortex dynamics, lock-in effect, and unsteady force generation. Phase-locked particle image velocimetry (PIV) was conducted at two reduced frequencies of 0.19 and 0.38. At the lower reduced frequency, asymmetric vortex shedding prevents synchronization between shedding and plunge motion frequencies, whereas at the higher reduced frequency, lock-in occurs with periodic shedding of separated leading- and trailing-edge vortices. Compared with previously studied surging motion under identical conditions, plunging requires a higher frequency to achieve lock-in and produces weaker wakes that break down more quickly downstream. Additionally, the aerodynamic load is extracted from the PIV flow field. For the plunging motion, the aerodynamic loads are dominated by pressure forces, with a maximum streamwise coefficient of approximately four times the static value at 90° angle of attack. This contrasts with the surging motion, where higher force variations are observed, and both pressure and mean momentum convection play comparable roles in the overall force. These results indicate that lock-in behavior depends strongly on both motion frequency and kinematics, where the effective angle of attack variation and the resulting vortex dynamics also determine whether synchronization can occur.

1 Introduction

Wind energy has emerged as one of the most powerful and rapidly growing renewable sources. As a result, wind turbines continue to scale in size, with projected onshore rotor diameters of approximately 270 m by 2030, which is more than 20% larger than current designs (GWEC 2024). This also means that their structural reliability under unsteady aerodynamic loading has become an increasingly critical concern.

Among the key challenges associated with turbine upscaling is vortex-induced vibration (VIV), which can significantly affect blade fatigue, structural integrity, and operational efficiency. VIV occurs when the vortex shedding frequency synchronizes with the natural frequency of the structure, resulting in large-amplitude oscillations and fluctuating aerodynamic loads (Williamson and Govardhan 2004). Although VIV has been extensively investigated in various engineering fields, such as bridges, offshore platforms, and cables (Bearman 1984; Williamson and Roshko 1988; Sarpkaya 2004), its implications for wind turbine blades have only recently gained attention. Modern long and slender blades, particularly under parked or installation conditions, may experience extreme pitch angles (e.g., up to 88.3° as observed at the Belwind wind farm (Shirzadeh et al. 2015)), which can exacerbate VIV-induced structural responses.

Recent studies have begun addressing VIV phenomena in large wind turbine blades. Horcas et al. (2020, 2022) demonstrated that inflow angle and tip geometry strongly influence VIV behavior, and proposed aerodynamic flaps as potential suppression devices (Horcas et al. 2018). Skrzypiński et al. (2016) investigated integral loading using detached eddy simulations (DES), emphasizing the dependence of prediction accuracy on inflow conditions.

At the airfoil level, the forced motion approach is commonly employed to study VIV lock-in phenomena, since free vibration responses are often affected by variable added mass and non-stationary frequencies (Sarpkaya 2004). In this framework, the airfoil oscillates at prescribed amplitudes and frequencies, enabling systematic analysis of lock-in behavior. Lock-in occurs when the vortex shedding frequency during forced motion matches the motion frequency. A num-

✉ Guanqun Xu
G.Xu-1@tudelft.nl

[1] Department of flow physics and technology, Delft University of Technology, Kluyverweg 1, 2629 HS Delft, South-Holland, The Netherlands

Published online: 25 May 2026

ber of studies (Besem et al. 2016; Benner et al. 2019; Meskell and Pellegrino 2019; Hu et al. 2021; Zou et al. 2015) have explored the influence of mean angle of attack, oscillation frequency, amplitude, and Reynolds number on vortex shedding synchronization of an airfoil. The lock-in region is typically represented as a V-shaped boundary (Besem et al. 2016; Meskell and Pellegrino 2019; Hu et al. 2021), as illustrated in Fig. 1, where the x-axis denotes the frequency ratio (r) between the airfoil motion (f_{pitch} or f_{plunge}) and vortex shedding frequency of a non-moving airfoil (f_{vs}), and the y-axis denotes the pitching amplitude for the pitch motion (Fig. 1a) or amplitude ratio between the motion amplitude and the airfoil chord for the plunge motion (Fig. 1b). Inside this V-shaped region (the shaded area), the vortex shedding frequency locks onto the motion frequency. For small amplitude (ratios), only values of r close to 1 induce the lock-in; instead, for higher amplitude (ratios), the lock-in occurs over a wider range of motion frequencies.

While most of the VIV studies have broadly investigated the lock-in phenomenon with the focus on motion frequency, force variations, and overall aerodynamic response, which provide valuable guidelines for VIV thresholds and mitigation strategies, a fundamental understanding of the underlying aerodynamics during VIV remains incomplete, as prior work has not thoroughly examined the transient flow physics governing lock-in mechanisms. This knowledge gap leaves critical questions unanswered about VIV.

More recently, Pirrung et al. (2024) reported that when a rotor is subjected to an 80° pitch and 90° yaw, VIV can trigger either flapwise or edgewise vibrations on different blades. This work leads to the need to understand directional differences in VIV behavior. Previously, Xu et al. (2025) experimentally examined a surging airfoil at 90° angle of attack and found that although the vortex dynamics differ significantly between frequency ratios $r = 0.39$ and $r = 0.78$, in both cases, lock-in happens. Although lock-in is typically expected at high r, it is also observed at low r (approximately 0.5), corresponding to a subharmonic condition consistent with Choi et al. (2015). Meanwhile, at these large angles of attack, the surging motion corresponds to the forced motion of a flapwise vibration; the corresponding behavior for plunging airfoils, representative of edgewise vibrations, remains largely unexplored, particularly at large angles of attack relevant to parked blade conditions.

The objective of this study is therefore to investigate the vortex dynamics, frequency lock-in, and aerodynamic loading of a plunging airfoil at large angles of attack. Specifically, an airfoil oriented at 90° angle of attack is forced to oscillate in the crossflow direction, corresponding to the edgewise vibration direction of a parked wind turbine blade. The study aims to understand the influence of motion direction on VIV mechanisms and complements the previous surging airfoil study (Xu et al. 2025) on the vortex dynamics and unsteady aerodynamic loading. The remaining paper is structured as follows: Sect. 2 describes the experimental methodology and data analysis method, Sect. 3 presents the results and discussion, and Sect. 4 reports the conclusion.

2 Methodology

2.1 Experimental setup

Measurements were performed in the Open Jet Facility (OJF) of Delft University of Technology. The OJF is a closed-circuit wind tunnel equipped with an open test section of octagonal shape, measuring 2.85 × 2.85 m.

Stereoscopic phase-locked PIV measurements were performed to evaluate the flow fields surrounding the wing. The PIV setup is shown in Fig. 2. This experiment employs a setup similar to that used for the surging airfoil investigation described by Xu et al. (2025). The primary difference lies in the orientation of the slider–crank mechanism (marked by the dashed rectangle in the left panel of Fig. 2). For the plunging motion considered here, the mechanism is mounted vertically to generate the desired crossflow motion, whereas in the surging configuration it was oriented horizontally. The key parameters for the PIV setup are listed in Table 1. The standard uncertainty of the phase-averaged flow velocity is $\varepsilon_u \approx 0.7\%$, and the uncertainty of the root mean square (RMS) of the velocity fluctuations is $\varepsilon_{u'} \approx 0.5\%$ (Xu et al. 2025).

The key experimental parameters are summarized in Table 2, while further details can be found in Xu et al. (2025), where the surging motion shares the same parameters. It is important to note that we set up the plunging motion amplitude to be $1.1c$ (corresponding to an amplitude ratio of 110%), which lies well beyond the range of amplitude ratios investigated by Hu et al. (2021). However, in the study from Heinz et al. (2016), it was found that with a certain combination of inflow inclination angles and inflow wind speed, VIV can be triggered with the tip deflection of more than one tip chord length. Therefore, although this range is outside the test range from the previous study (Fig. 13l), it holds importance in the wind energy industry.

In order to check the validity of our two test cases, namely, the low-frequency case with $f = 2.5$ Hz, $k = 0.19$, and the high-frequency case with $f = 5$ Hz, $k = 0.38$, we compare our parameter space with the VIV conditions presented in Govardhan and Williamson (2000). Under the condition of a free vibrating cylinder, the case with $f = 2.5$ Hz, $k = 0.19$, is located in a higher-reduced-velocity region where lock-in does not happen with such a high motion amplitude of $1.1c$. However, for the higher-frequency case, our test case is located very close to the upper branch, where VIV happens at high motion amplitudes of approximately $1c$. Therefore,

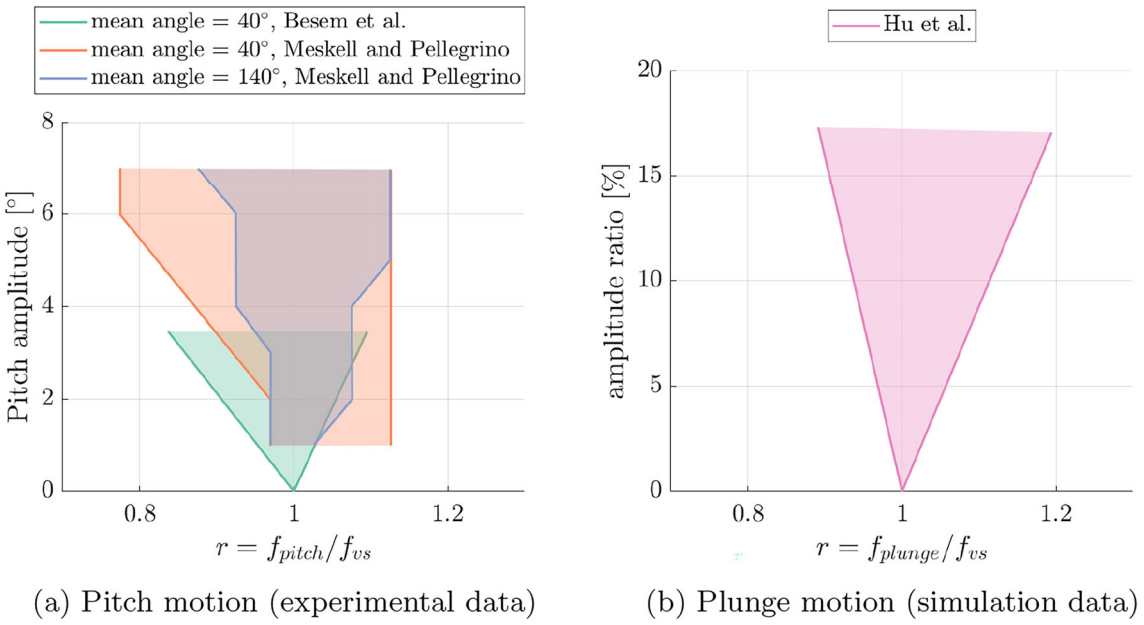

Fig. 1 V-shaped lock-in region adapted from Besem et al. (2016), Maskell and Pellegrino (2019) for the pitch motion, and Hu et al. (2021) for the plunge motion

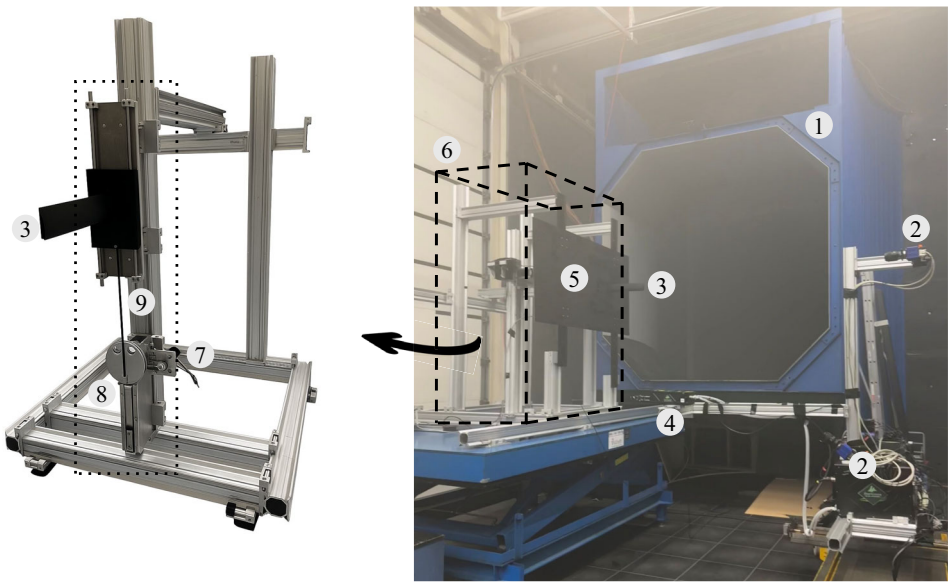

Fig. 2 Experimental setup in the OJF. The relevant components are: 1. Flow outlet 2. LaVision Imager sCMOS camera 3. Wing model 4. Quantel Evergreen Nd:YAG laser 5. Base plate 6. Beam structure (including the slider–crank mechanism) 7. Motor 8. Turning wheel 9. Rod for straight motion

by comparing them with classical cylinder VIV conditions, these two design cases are important both in their comparison and in their application under airfoil forced vibration conditions.

The airfoil profile NACA 0021 was selected for the experimental measurement. Although not commonly used in modern horizontal-axis wind turbines, it remains an appropriate choice for this investigation for two primary reasons. First, under the high angle of attack conditions considered, the flow physics are dominated by vortex shedding from the leading and trailing edges. Consequently, the specific aerodynamic curvature becomes minor to the global flow dynamics. Second, the NACA 0021 is a commonly used shape in aerodynamic and aeroelastic literature, which provides a robust baseline for characterizing fundamental behavior. The results obtained in this study are compared to static experimental data, for example, from Holst et al. (2019). Please refer to Sect. 3.2 for further details.

It is worth mentioning that the angle of attack AoA_g is defined as the angle between the incoming wind and the airfoil chord line, which is always 90° for both the plunging motion (the present study) and the surging motion (Xu et al. 2025). However, the effective angle of attack, which is the angle between the chord line and the relative wind speed

Table 1 Summary of stereoscopic phase-locked PIV setup and parameters

Category	Parameter	Specification/description
Seeding	Tracer particle	Water–glycol droplets generated by SAFEX smoke generator
	Particle size	Median diameter $\approx 1\ \mu$m
Illumination	Laser type	Quantel Evergreen Nd:YAG, double-pulse system
	Pulse energy	200 mJ per pulse
	Wavelength	532 nm (green)
	Field of View (FoV)	269.4 × 331.8 mm ($\approx 3.6c \times 4.4c$), extended to $8c \times 4.2c$ by traversing
Imaging	Camera model	LaVision Imager sCMOS (2 units)
	Sensor size	2560 × 2160 pixels
	Pixel pitch	6.5 × 6.5 µm
	Time separation (Δt)	417 µs between image of a pair
	Sampling frequency	2.5 Hz and 5 Hz (equal to motion frequency)
	Method	Phase-locked (realized by optical encoder)
	No. image pairs	200 per phase
	No. phases	12 per plunging cycle
Optics	Lens focal length	105 mm (Nikon)
	Numerical aperture (f/#)	f/8
	Measurement plane	Located at $3c$ from the wing tip
Data processing	Interrogation window	32 × 32 pixels (3.37 mm × 4.92 mm)
	Overlap factor	75%
	Vector pitch	$\approx$ 1.0 mm

Table 2 Experimental parameters

Parameter	Symbol	Value
Free-stream velocity	U_∞	3.1 m/s
Airfoil profile		NACA 0021
Model chord	c	0.075 m
Reynolds number	Re	1.5×10^4
Static vortex shedding frequency[a]	$f_{st,90}$	6.4 Hz
Angle of attack	AoA_g	90°
Model span	s	0.4 m
Model aspect ratio	AR	5.33
Motion frequency	f	2.5 Hz, 5 Hz
Reduced frequency	k^b	0.19, 0.38
Frequency ratio	$f/f_{st,90}$	0.39, 0.78
Motion amplitude	h_{max}	0.083 m (1.1c)

[a] Measured at AoA = 90°
[b] $k = 2\pi f(c/2)/U_\infty$(Leishman 2006)

(composed of the incoming wind and the perceived wind speed in the crossflow direction) is different for the plunging case, which will be discussed in Sect. 2.2.

2.2 Motion kinematics

The wing's motion kinematics are shown in Fig. 3a, where the wing's actual motion amplitude h is obtained by physically tracking the airfoil leading-edge position from the phase-averaged PIV images. The velocity $\dot{h}$ and acceleration $\ddot{h}$ of the motion were obtained by taking temporal derivatives of the fitted wing position data ($h = 0.0616 \sin(\phi - 5.7) + 0.015$, the dashed line with the cross markers in the top figure in Fig. 3a). The airfoil relative location at three intermediate phases of 0°, 90°, and 270° is shown in Fig. 3b. The origin is located at the plunging axis; at $\phi = 0°$, the leading edge is located at $y = -0.78c$, and the trailing edge is located at $y = 0.22c$.

Compared to a surging motion, where the wing moves in the same direction as the wind, which does not change the effective angle of attack at 90°, a plunging wing experiences a varying effective angle of attack, even though its physical orientation remains at 90° ($\text{AoA}_g = 90°$). As shown in Fig. 4, the effective angle of attack (AoA) is determined by the combination of the free-stream velocity (U_∞) and the velocity component induced by the airfoil's vertical motion ($\dot{h}$), which acts in the opposite direction to the motion in the crossflow.

$$\text{AoA} = \begin{cases} \arctan\left(\frac{U_\infty}{|\dot{h}|}\right), & \text{if } \dot{h} \le 0, \\ \arctan\left(\frac{\dot{h}}{U_\infty}\right) + 90°, & \text{if } \dot{h} > 0. \end{cases} \quad (1)$$

The effective angle of attack within a plunging cycle is plotted in Fig. 5 for both motion cases. For $k = 0.38$ case, the variation of AoA is larger, ranging from approximately 58° to

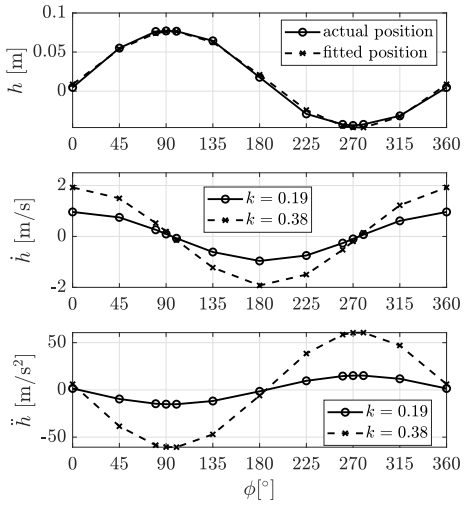

(a) The actual motion amplitude (h) based on the leading edge of the airfoil, velocity ($\dot{h}$), and acceleration ($\ddot{h}$) of the plunging motion for two motion frequencies. Note that the lines for h overlap each other since two cases have the same travel distance.

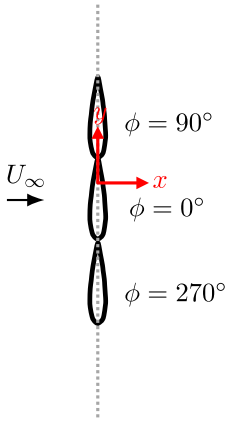

(b) The relative locations of the airfoil at three different phases: $\phi = 0°$, where the wing is near the center of its trajectory, $\phi = 90°$, and $\phi = 270°$, where it is in the most top and bottom positions, respectively.

Fig. 3 Motion kinematics of the plunging airfoil

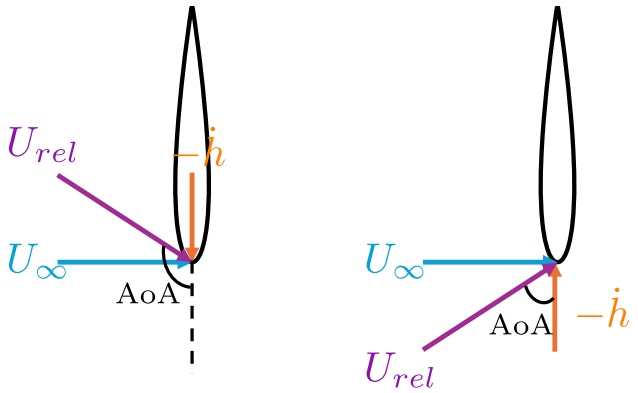

Fig. 4 Illustration of the effective angle of attack AoA during upstroke (left) and downstroke (right). U_{rel} represents the relative velocity experienced by the airfoil

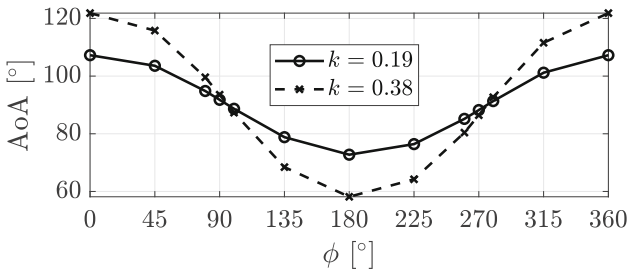

Fig. 5 Effective angle of attack at different phases for two motion frequency cases during plunging

122°, while that for $k = 0.19$ is between 73° and 108°. Note that due to the varying angle of attack, the frequency ratio listed in Table 2 is the ratio between the motion frequency and static vortex shedding frequency at 90° angles of attack, where the latter was obtained through the POD analysis as discussed in Xu et al. (2025).

2.3 Airfoil wake topology

Due to the varying effective angle of attack, the wake exhibits a periodic skewness during the plunging cycle. To quantify this behavior, the wake skew angle is defined in two steps.

First, the center of the wake at each streamwise plane, $y_w(x)$, is determined using the center-of-mass method, which has also been applied in wind turbine wake studies (Ajay and Ferreira 2024; Bensason et al. 2025). The center of the wake $y_w(x)$ is expressed as

$$y_w(x) = \frac{\int_{\Omega(x)} y\left[U_\infty - \bar{u}(x,y)\right] \mathrm{d}y}{\int_{\Omega(x)} \left[U_\infty - \bar{u}(x,y)\right] \mathrm{d}y}, \tag{2}$$

where $\Omega(x) = \{\, y : \bar{u}(x,y) \le U_\infty \,\}$ and $\bar{u}(x,y)$ is the time-averaged flow velocity, meaning the y region is limited to the wake of the airfoil. For the discrete experimental measurement, the integrals in Eq. 2 are computed by summing the velocity difference ($U_\infty - \bar{u}(x,y)$) (or the product of the y-

location and the velocity difference) over the PIV grid points within $\Omega(x)$.

Next, the local wake skew angle (in degrees) is calculated as

$$\gamma(x_i) = \arctan\left(\frac{\Delta y_w}{\Delta x}\right) = \arctan\left(\frac{y_w(x_{i+1}) - y_w(x_i)}{x_{i+1} - x_i}\right) \quad (3)$$

In this study, $\gamma = 0°$ corresponds to a wake aligned with the free-stream velocity U_∞. A positive skew angle ($\gamma > 0$) indicates an upward deflection of the wake, while a negative skew angle ($\gamma < 0$) corresponds to a downward deflection.

2.4 Definition of lock-in in the context of phase-locked PIV

The definition for the lock-in under forced plunging motion is the frequency match between the vortex shedding and the forced motion (Bishop and Hassan 1964; Besem et al. 2016). In this study, this frequency match is identified through the vorticity fields from the phase-locked PIV measurements.

If, during one plunging cycle (containing 12 measured phases), the pair of vortices experiences one cycle of growth and shedding, then the vortex shedding cycle matches the motion cycle, which is considered locked in. However, if during one plunging cycle, multiple vortex shedding events occur, there is no lock-in between motion frequency and vortex shedding frequency.

2.5 Load estimation from PIV results

The load during the plunging motion is estimated from the PIV flow field. First, the resulting pressure fields from PIV flow results are achieved by applying the Reynolds averaged Navier–Stokes equation, and then solving for the static pressure using the Poisson equation formulation, as described by van Oudheusden (2013). The boundary conditions used in the computations are defined as follows. At the inlet (the left boundary of the PIV flow field), a Dirichlet boundary condition is applied, with the pressure specified according to the Bernoulli equation. For all other boundaries, including the top, bottom, and right edges of the PIV flow field, as well as the airfoil's internal surface, Neumann boundary conditions are employed, with the pressure gradients calculated from the Navier–Stokes equations.

Second, for two-dimensional flows, the aerodynamic forces can be evaluated using the momentum conservation around a control contour enclosing the airfoil (Rival and Oudheusden 2017). In this study, an arbitrary rectangle contour **C** is applied, as shown in Fig. 6.

Following the methodology of Ragni et al. (2011), van de Meerendonk et al. (2016), and Rival and van Oudheusden (2017), the force integration is written as:

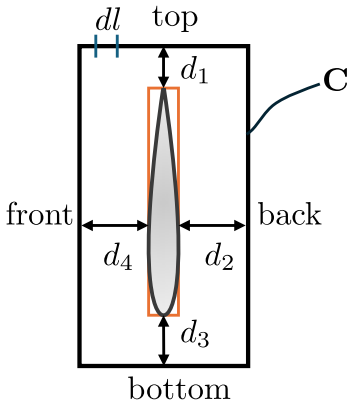

Fig. 6 Illustration of the control boundary **C** used for the load integration. d_1 to d_4 represent the distance between the boundary and the airfoil surface from the top, back, bottom, and front, respectively

$$\begin{aligned}\bar{F}_i = &-\rho \tfrac{\partial}{\partial t} \oint_C \bar{u}_i n_j x_j \,\mathrm{d}l - \rho \oint_C \bar{u}_i \bar{u}_j n_j \,\mathrm{d}l \\ &-\rho \oint_C \overline{u_i' u_j'} n_j \,\mathrm{d}l - \oint_C \bar{p} n_i \,\mathrm{d}l \\ &+\rho \nu \oint_C \left(\tfrac{\partial \bar{u}_i}{\partial x_j} + \tfrac{\partial \bar{u}_j}{\partial x_i}\right) n_j \,\mathrm{d}l \end{aligned} \quad (4)$$

Here, $\bar{u}_i$ denotes the time-averaged velocity component in the i-direction for the static case or phase-averaged for the plunging case, $\overline{p}$ is the corresponding time- or phase-averaged pressure, ν is the kinematic viscosity, ρ is the air density, and $\overline{u_i' u_j'}$ represents the Reynolds stress tensor. dl is the element length on the contour, with outward-pointing normal vectors n_i and n_j. From left to right, the terms in Eq. (4) correspond to contributions from flow unsteadiness, mean momentum convection, turbulent momentum transfer, pressure, and viscous stresses.

For phase-locked PIV measurements with a fixed field of view, the unsteadiness term simplifies to:

$$-\rho \frac{\partial}{\partial t} \oint_C (x_i \, \bar{u}_i \, n_i) \,\mathrm{d}l = -\rho \oint_C \left(x_i \frac{\partial \bar{u}_i}{\partial t} n_i\right) \mathrm{d}l \quad (5)$$

where $\partial \bar{u}_i / \partial t$ is obtained from consecutive phases:

$$\frac{\partial \bar{u}_i}{\partial t} = \frac{\partial \bar{u}_i}{\partial \phi_k} \frac{\partial \phi_k}{\partial t} \approx \frac{\bar{u}_{i,k+1} - \bar{u}_{i,k-1}}{\phi_{k+1} - \phi_{k-1}} 2\pi f \quad (6)$$

with $\phi_k = 2\pi f t_k$ denoting the kth measured phase and $\bar{u}_{i,k\pm1}$ the velocities at adjacent phases.

However, Eq. 4 assumes an incompressible flow and a thin body (Rival and Oudheusden 2017). For the NACA 0021 airfoil at 90° AoA, acting as a bluff body, an additional body force must be included:

$$F_B(t) = -\rho B \ddot{h} \quad (7)$$

where B is the cross-sectional area of the airfoil.

The control boundary, illustrated in Fig. 6, is defined as a rectangular region enclosing the airfoil. The rectangular geometry was selected arbitrarily, serving as a convenient and consistent boundary for the control volume analysis. For both frequency cases, a total of 14 different control boundaries were employed to compute averaged quantities and their associated uncertainties. The boundary dimensions were varied such that $d_1 = d_2 = d_3 = d_4$, ranging from $10\,dx$ to $23\,dx$ with an interval of dx, where $dx = 0.027c$ denotes the vector spacing within the measured FoV.

2.5.1 Load estimation of the surging cases with the same control boundaries

In order to make a fair comparison of the aerodynamic load between the plunging motion (the present study) and the surging motion (Xu et al. (2025)), the control boundaries for the force integration should have the same range. Note that for the surging cases discussed in Xu et al. (2025), $d_1 = d_2 = d_3 = d_4$, ranging from $10\,dx$ to $30\,dx$. However, due to the limitation of the FoV in the crossflow direction, the control boundary for the plunging case cannot reach more than $23\,dx$. Therefore, for the result of the surging cases, the same control boundaries as the plunging cases are set ($d_1 = d_2 = d_3 = d_4$, ranging from $10\,dx$ to $23\,dx$ with an interval of dx).

3 Results and discussions

3.1 Vortex dynamics and vorticity

3.1.1 The low-frequency case: $k = 0.19$

The streamwise velocity fields at different measured phases are shown in Fig. 7 for the $k = 0.19$ ($f/f_{st,90} = 0.39$) case. The phases are shown in the order of trailing-edge vortex (TEV) formation and shedding. The wake centers are calculated using Eq. 2 and Eq. 3 and are plotted with a black circled line, with the calculation starting at $x/c = 0.1$ and extending up to $x/c = 3$. Compared to the static measurement as shown in Xu et al. (2025), the velocity fields at each measurement phase show high similarities: A suction region is generated downstream of the airfoil (highest suction centered between $x/c = 1$ to 3 for this plunging case) while accelerated flow is formed downwind of the airfoil outside of the wake region (shown as deeper red color in Fig.7). The plunging case at $k = 0.19$ shows higher flow velocity in this region than the static case because the airfoil's vertical motion increases the local relative flow speed near the airfoil. The wake skew angle distribution is shown in Fig. 8a for the $k = 0.19$ case. For each phase, γ remains nearly constant up to $x/c \approx 2$. Beyond this point, noticeable variations occur, especially at $\phi = 80 - 135°$ and 225°, where the standard deviation reaches up to $\pm 15.9°$ (at $\phi = 100°$) within the $3c$ downstream position. This high variation is closely associated with the high crossflow aerodynamic force (not shown here) during these phases, which is caused by asymmetric vortex shedding and wake deformation. The vortex dynamics are discussed in the following paragraphs.

The spanwise vorticity contour at $k = 0.19$, as shown in Fig. 9, exhibits the evolution of the vortices in the plunging cycle. The phases also follow the order of the TEV formation and shedding. The cycle starts from $\phi = 180°$, where the airfoil is near the center of the travel and moving down. The starting vortex at the trailing edge is established, and its non-dimensionalized circulation $\frac{\Gamma}{U_\infty c}$ is -1.94, as shown in Fig. 10. As the airfoil plunges down to $\phi = 225°$ (Fig. 9b), 260° (Fig. 9c), and 270° (the lowest location, Fig. 9d), the vortex grows and the magnitude of Γ increases steadily, where $\frac{\Gamma}{U_\infty c}$ reaches -3.0 at $\phi = 270°$. Subsequently, as the airfoil begins its upward motion, the wake gradually reorients from being directed upward (e.g., averaged $\gamma \approx 21°$ at $\phi = 180°$) to nearly parallel to the inflow at $\phi = 280°$ (Fig. 9e, $\gamma \approx 2.8°$) and $\phi = 315°$ (Fig. 9f, $\gamma \approx -6.3°$), to being directed downward at $\phi = 0°$ (Fig. 9g, $\gamma \approx -17.0°$) and $\phi = 45°$ (Fig. 9h, $\gamma \approx -22°$). During this period from $\phi = 270°$ to $\phi = 315°$, the TEV circulation magnitude continues to increase, fed by the boundary layer, while the TEV adopts a more diffused structure. However, when the airfoil reaches $\phi = 80°$ (Fig. 9i), the elongated TEV exhibits a discontinuity. The portion of the TEV located upstream of $x/c \approx 2$ follows the airfoil motion closely and is oriented with a small γ of approximately $\approx -10.0°$. In contrast, in the region of $x/c > 2$, a smaller γ of lower than $-20°$ is shown in Fig. 8a, meaning the rear part of the wake is skewed more downward. The rear portion of the TEV, located downstream of $x/c \approx 2$, remains almost stationary and lies below $y/c \approx 1$. At this phase, the airfoil's vertical velocity is relatively small ($\dot{h} = 0.5$ m/s), while its acceleration is significant ($\ddot{h} = -58.5$ m/s^2). Consequently, the rear portion of the TEV, located downstream of $x/c \approx 2$, does not immediately follow the airfoil motion. The fluid responds slowly to the changing flow due to the inertia, causing it to lag behind the upstream portion; this lag manifests as a larger negative skew angle ($\gamma < -20°$) and keeps the rear TEV nearly stationary below $y/c \approx 1$. When the airfoil moves up to $\phi = 90°$ (the highest point, Fig. 9j) and then down to $\phi = 100°$ (Fig. 9k) and $\phi = 135°$ (Fig. 9l), the airfoil changes its motion direction with high acceleration (as shown in Fig. 3a), the part of the TEV with $x/c > 2$ cannot maintain its motion with the airfoil and starts to separate from the trailing edge, and convects into the wake at $\phi = 135°$ (marked in Fig. 9l). At $\phi = 180°$, traces of the separated vortex (the medium blue colors) of the TEV between

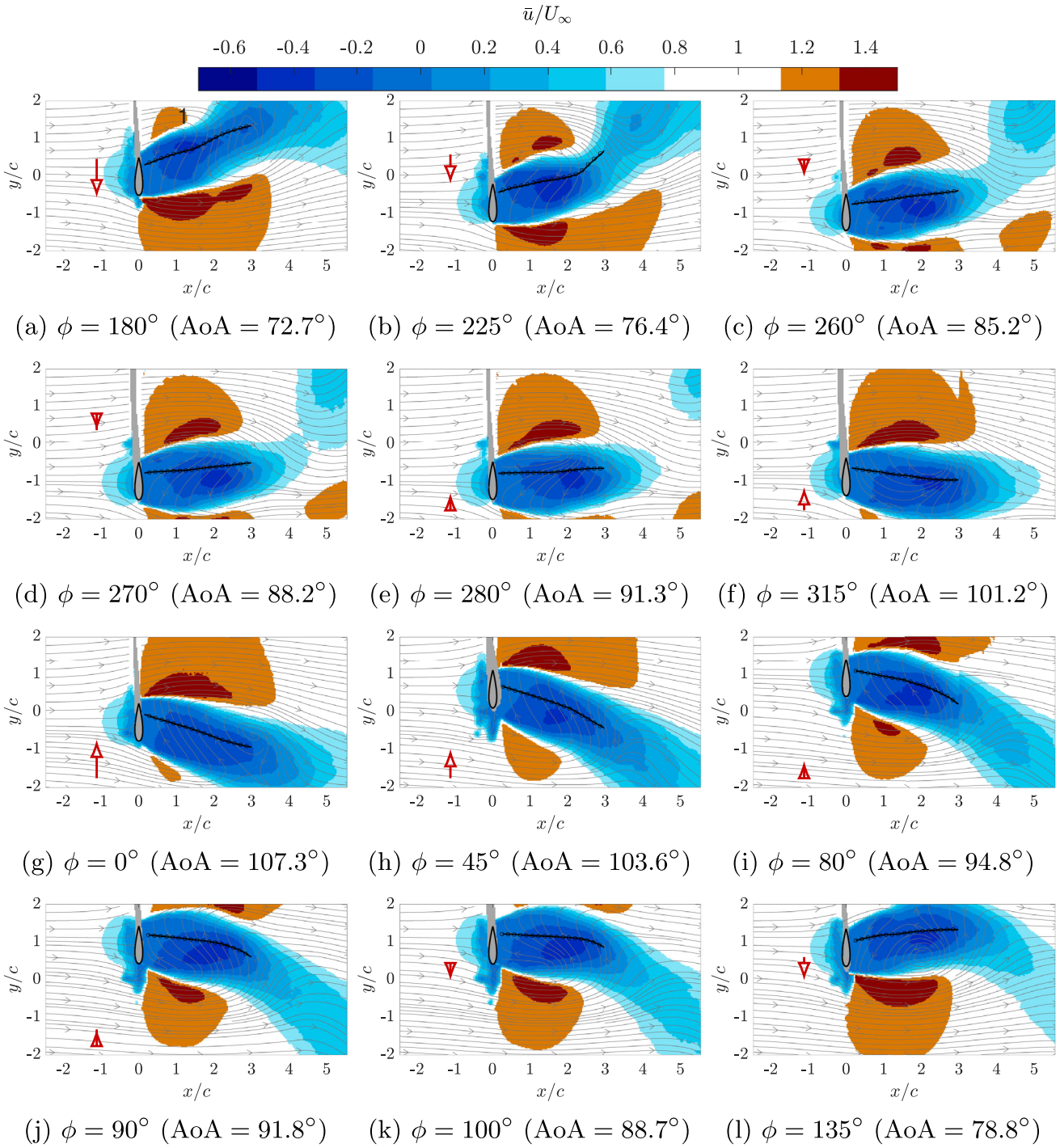

Fig. 7 Streamwise velocity field $\bar{u}/U_\infty$ for $k = 0.19$ plunging case at all measured phases. The red arrow represents the scaled motion velocity $\dot{h}$. The wake center line is marked by the black circled line

$x/c = 3$ and 5 are shown, where in the front ($x/c < 2$) the new cycle begins.

On the contrary, the leading-edge vortex (LEV) exhibits a different timing in its formation and shedding during the plunging motion at $k = 0.19$. Interestingly, the LEV separation occurs twice during one plunging cycle. The first one happens from $\phi = 225°$ (Fig. 9b, with the separated LEV marked by the red dashed circle) to 260° (Fig. 9c), where $\frac{\Gamma}{U_\infty c}$ decreases from 4.6 to 2.7, as shown in Fig. 10. This LEV separation is followed by the TEV separation from the previous phases from $\phi = 135°$ (Fig. 9l) to 180° (Fig. 9a), which results in the formation of a separated vortex pair.

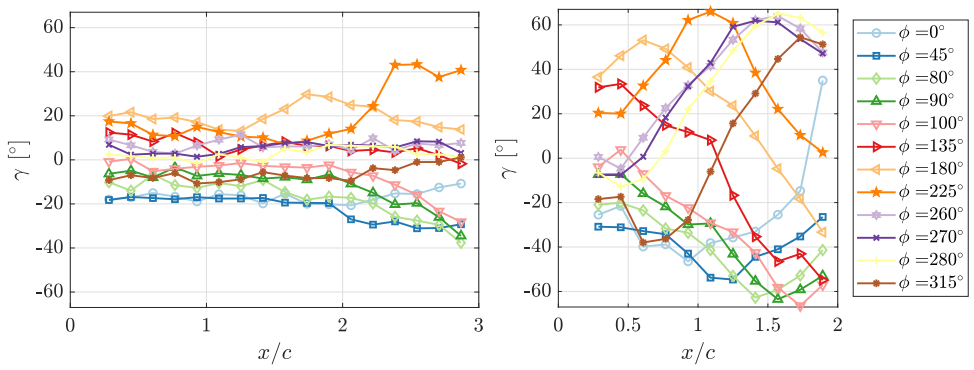

(a) $k = 0.19$ (b) $k = 0.38$

Fig. 8 Wake skew angle distribution γ at different phases

Meanwhile, it is also observed that between $\phi = 315°$ (Fig. 9f), $\phi = 0°$ (Fig. 9g), and $\phi = 45°$ (Fig. 9h), the LEV evolves from extending to approximately $x/c = 4.5$ at $\phi = 315°$, to exhibiting a discontinuity near $x/c = 3$ at $\phi = 0°$, and finally to forming a shorter structure terminating before $x/c = 3$ at $\phi = 45°$. Although the FoV is insufficient to directly capture the complete shedding process, these observations provide strong evidence that the LEV undergoes separation during this interval: It is shown that among the three phases ($\phi = 260°$ to $280°$), the LEV continues to accumulate circulation, and the LEV elongates in the streamwise direction. Due to the change in airfoil motion direction from $\phi = 270°$ to $\phi = 280°$ and $\phi = 315°$, the wake changes its averaged skew angle (before $x/c = 2$) from 4.8° to 2.3°, and −8.2° (tilting down). This change causes the LEV to stretch from an upward-pointing orientation to a downward-pointing one (marked by the dashed arrows in the plots). At the same time, when the airfoil advances to $\phi = 0°$ (near the center of travel, moving upward), the TEV grows in size and dissipates to a larger area into the wake region, with the lowest point of y/c near $x/c = 3$. The induced velocity from the expanding TEV modifies the local pressure distribution around the LEV, eventually contributing to its detachment. As a result, this LEV separation occurs at the part of the LEV of approximately $x/c = 3$. After this process, the TEV develops further (with $\frac{\Gamma}{U_\infty c}$ decreasing to −4.3), as illustrated at $\phi = 45°$ (Fig. 9h).

Therefore, during a plunging cycle at $k = 0.19$, the airfoil exhibits periodic vortex shedding characterized by two distinct events: A primary vortex pair (one LEV and one TEV) separates from the front part during the downstroke, followed by an additional LEV separation during the upstroke. During this second event, the TEV continues to grow, fed by the separating boundary layer rather than shedding into the wake. This behavior indicates that at this reduced frequency and frequency ratio ($f/f_{st,90} = 0.39$), vortex shedding follows a more complex mechanism instead of locking into the motion frequency. This result contrasts with the surging case at the same k reported by Xu et al. (2025), where lock-in occurs. In surging motion, the purely streamwise oscillation modulates only the effective velocity amplitude while maintaining a constant angle of attack, preserving flow symmetry and enabling synchronization between vortex shedding and motion. In contrast, plunging motion introduces a transverse velocity component that causes a time-varying effective angle of attack (see Fig. 5). The resulting flow asymmetry leads to complex vortex dynamics and multiple separation events per cycle, including the additional LEV separation observed here. Furthermore, based on previous studies (Fig. 1), $f/f_{st,90} = 0.39$ lies in a regime where lock-in is less likely compared to higher f/f_{st} values (close to 1). Consequently, while the surging case exhibits subharmonic lock-in, this phenomenon fails to emerge in the plunging case due to the inherent flow asymmetry and continuous variation in the effective angle of attack.

3.1.2 The high-frequency case: $k = 0.38$

The velocity contour for $k = 0.38$ ($f/f_{st,90} = 0.78$) case is shown in Fig. 11. The wake centers are plotted using a black circled line, with the calculation starting at $x/c = 0.1$ and extending up to $x/c = 2$. The streamwise velocity field exhibits a different wake characteristic compared to the $k = 0.19$ case. A notable difference lies in the spatial difference of velocity magnitudes. For $k = 0.38$, the wake velocity peaks in the immediate near-wake region (approximately within $1c$ downstream), while for $k = 0.19$, the high-magnitude region extends further up to approximately $4c$ from the airfoil. This difference arises from the larger variation in motion velocity and AoA at $k = 0.38$. The corresponding high oscillation frequency shortens the streamwise wavelength of the vortex structures, effectively confining them to a shorter region downstream. This manifests as a concentrated near-wake local velocity gradient. Conversely, the milder AoA variations at $k = 0.19$ allow vortices to con-

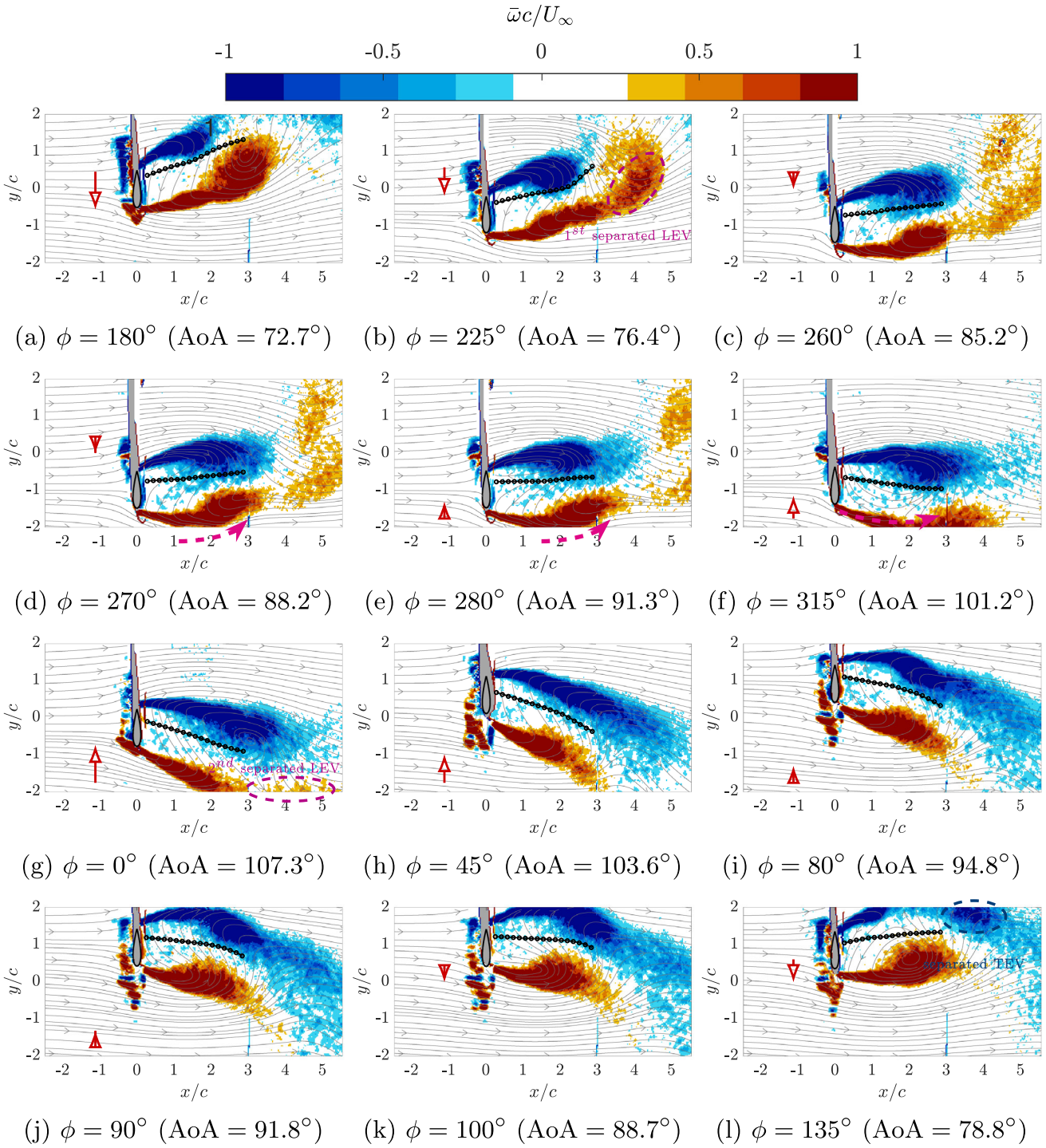

Fig. 9 Contours of the phase-averaged spanwise vorticity component superimposed with streamlines. Vortex identified using Γ_1 method for the $k = 0.19$ surging case. The red arrow represents the scaled motion velocity $\dot{h}$. The wake center line is marked by the black circled line

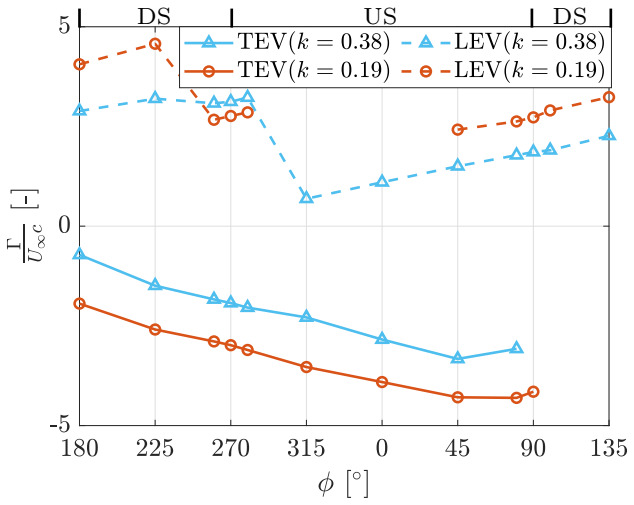

Fig. 10 Non-dimensionalized circulation $\frac{\Gamma}{U_\infty c}$ of the LEV and TEV at different phases in a cycle, obtained using the method from Xu et al. (2025). The upstroke (US) and downstroke (DS) periods are marked on top of the figures with US defined as the wing moving up and DS as the wing moving down

vect further downstream, resulting in a larger area of reverse flow region and a more elongated wake.

In addition, at the higher frequency ($k = 0.38$), the wake displays a wavier pattern with discontinuous structures in the near-wake region ($x/c \approx 1.8$), as evident from Fig. 11c–e. The wake skew angles γ at $k = 0.38$ are plotted in Fig. 8b for their streamwise distribution. It shows much higher overall variations between $-66°$ to $66°$ within a shorter x/c range of 0 to 2, while that for $k = 0.19$ is confined between $-40°$ and $50°$ over a longer wake extent of 0 to 3. For each phase, the variations of the wake skew angle are substantially higher compared to the $k = 0.19$ case. The highest variation at the high-frequency case occurs at $\phi = 315°$ with the standard deviation of $\pm 33.8°$, which is approximately 2.1 times higher than the low-frequency case. The wavier and more irregular wake at $k = 0.38$ results from a higher crossflow aerodynamic force (not shown here) compared to the $k = 0.19$ case, which in turn arises from stronger vortex interactions driven by rapid changes in effective angle of attack and increased flow unsteadiness. In Fig. 12, the variation of γ with AoA in the near-wake region is shown for both cases. For both cases, the γ at $x/c = 0.5$ is selected to plot as γ becomes very unstable after $x/c = 0.6$ for the higher-frequency case, as shown in Fig. 8b. Compared to the $k = 0.19$ case, the variation of AoA at $k = 0.38$ is about 1.8 times higher. Meanwhile, the variation of γ for the $k = 0.38$ case is approximately 2 times higher relative to $k = 0.19$. Therefore, the overall variation of the wake skew angle γ scales roughly proportionally with the variation of AoA, caused by the difference in k.

Figure 13 presents the spanwise vorticity contour at $k = 0.38$, following the TEV formation and shedding order. At $\phi = 180°$ (near the center of travel, moving down), the TEV starts to grow, with $\frac{\Gamma}{U_\infty c}$ starting from -0.7, as shown in Fig. 10. When the airfoil moves down to the lowest point ($\phi = 270°$, Fig. 13d) and then moves up to $\phi = 280°$ (Fig. 13e), the TEV remains close to the airfoil, with the most downstream boundary near $x/c = 1.5$. During this period, $\frac{\Gamma}{U_\infty c}$ from the TEV steadily decreases to approximately -2.0. As the airfoil continues its upward plunge to $\phi = 315°$ and $\phi = 0°$ (Fig. 13f and g), the TEV elongates streamwise and downward (marked by the dashed arrow), stretched by the high relative velocity due to the airfoil's upstroke motion. Then, as the airfoil plunges up to $\phi = 80°$ (Fig. 13i), the TEV becomes distorted near $x/c = 1.8$, nearly separating apart under the influence of the strengthening LEV, which is convecting downstream toward it (marked by the dashed arrow). As the airfoil moves up to $\phi = 90°$ (Fig. 13j) and $\phi = 100°$ (Fig. 13k), the rear part of the TEV gradually detaches from the front part. This occurs because the fluid in this region has low momentum (close to zero velocity near $x/c \approx 2.3$, $y/c \approx -0.5$, as shown in Fig. 11j and k) and responds slowly to the rapidly changing motion of the airfoil ($\ddot{h} \approx -60.5$ m/s^2 at $\phi = 90°$ and $100°$), preventing the rear vortex from immediately following the upstream flow and leading to its apparent separation. Meanwhile, when the airfoil moves further down to $\phi = 135°$ (Fig. 13l), the growing LEV elongates in the direction of the TEV (marked by the dashed arrow), which starts to separate the remaining rear part of the TEV. This separation process is finished at $\phi = 180°$. At this phase, the airfoil has the highest speed (pointing down), which also facilitates the shedding as the rear part has a relatively low speed compared to the airfoil. At this phase, the two rear parts of the TEV (including the one that remains stagnant between $\phi = 90°$ and $100°$) shed simultaneously, and a new TEV formation cycle begins.

On the other hand, a similar pattern can be found for the LEV development at $k = 0.38$. Instead, the growth of the LEV starts at $\phi = 315°$ where the $\frac{\Gamma}{U_\infty c}$ is 0.68. During the upstroke period until $\phi = 90°$ (the most top location), the LEV accumulates strength while maintaining close to the leading edge (the most downstream boundary maintains smaller than $x/c \approx 1.6$). Once the airfoil starts to move down from $\phi = 100°$ and onward, the LEV tilted upwards and elongates in the same direction (as shown in the dashed arrow in Fig. 13l). During this downstroke period between $\phi = 100°$ and $\phi = 270°$, the wake skew angle changes accordingly from $-32.0°$ (tilting down) to $34.0°$ (tilting up). When the airfoil moves down to $\phi = 270°$ (the bottommost location), the growth of the TEV similarly separates the rear part of the LEV (marked by the dashed arrow). Due to the fluid momentum in this region (low local velocity near $x/c \approx 2.5$, $y/c \approx 0$, shown in Fig. 11d and e), this rear portion cannot immediately follow the rapid motion of the airfoil ($\ddot{h} \approx 60.5$ m/s^2 at $\phi = 270°$ and $280°$), and it remains nearly

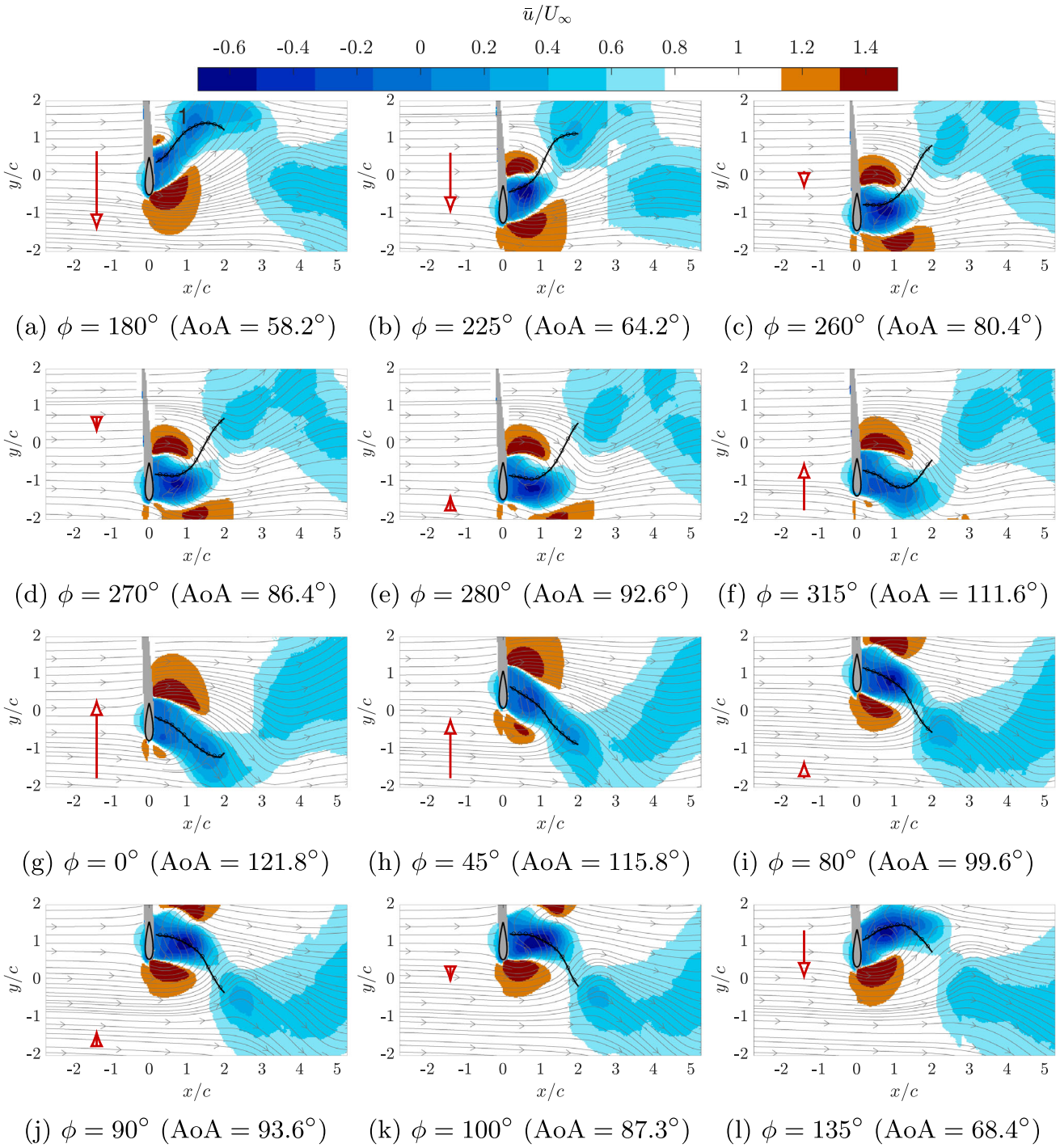

Fig. 11 Streamwise velocity field $\bar{u}/U_\infty$ for $k = 0.38$ plunging case at all measured phases. The red arrow represents the scaled motion velocity $\dot{h}$. The wake center line is marked by the black circled line

stationary in the wake until $\phi = 280°$. As the airfoil moves up to $\phi = 315°$ (Fig. 13f), the rear part of the remaining LEV (the 2^{nd} separated LEV) detaches due to the growing TEV, and sheds in the wake together with the first (stagnant) rear part of the vortex (the 1^{st} separated LEV), as also partially shown at $\phi = 0°$ (Fig. 13g).

Therefore, during a plunging cycle at $k = 0.38$, the large angle of attack variations characteristic of this motion generate complex LEV–TEV interactions, resulting in a highly distorted wake structure. This higher motion frequency also leads to smaller circulation magnitudes compared to the $k = 0.19$ case (Fig. 10). This strong flow interaction causes

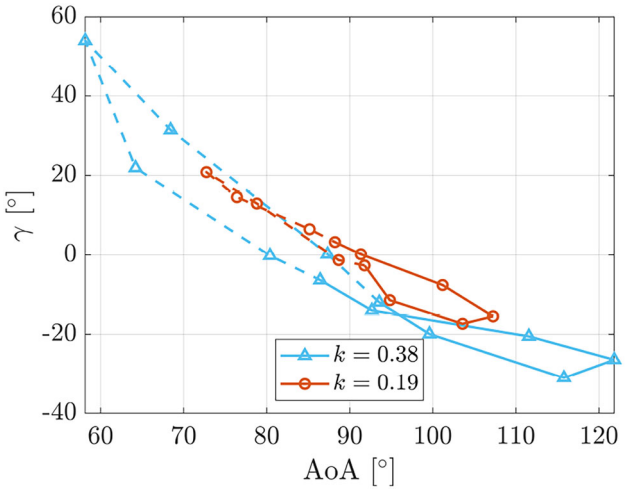

Fig. 12 Wake skew angle γ as a function of AoA at $x/c = 0.5$. The solid line indicates the upstroke process and the dashed lines indicate the downstroke process

mutual separation of both the LEV and TEV by their counterpart vortices prior to final detachment, where the frequency lock-in is manifested through the synchronized separation of two vortex pairs into the wake.

Compared to the surging motion discussed in Xu et al. (2025), both surging and plunging motions at $k = 0.38$ exhibit frequency lock-in with the imposed oscillation frequency, consistent with previous studies (Koopmann 1967; Anagnostopoulos 2000; Meneghini and Bearman 1995) for high frequency ratios. However, their distinct kinematics produce fundamentally different vortex shedding patterns. For the surging motion (streamwise oscillation), the fixed angle of attack at 90° leads to nominally symmetric development of the LEV and TEV, resulting in similar vortex structures and synchronous shedding. In contrast, the plunging motion (crossflow oscillation) induces a continuously varying angle of attack. This kinematic asymmetry amplifies the inherent geometric asymmetry between the rounded leading edge and sharp trailing edge: While the sharp trailing edge enforces immediate separation, the rounded leading edge allows partial flow attachment before separation. As a result, the timing of vortex formation and shedding differs between the two edges. Consequently, the LEV and TEV evolve with unequal strengths and distinct shapes (with additional LEV separation occurring at the lower-reduced-frequency case) and shed asynchronously, resulting in a consecutive vortex street. While this wake pattern bears some resemblance to those reported in oscillating cylinder studies, such as Lin et al. (2023), the present results reveal distinct differences arising from the airfoil kinematics. At higher k, the edge effect is minimized, producing two well-separated vortex pairs, whereas at lower k, additional LEV separation leads to imbalanced vortex shedding and prevents lock-in.

3.2 Load estimation

The load estimation approach introduced in Sect. 2.5 is applied to the plunging airfoil PIV flow field to estimate aerodynamic forces. The streamwise force coefficient, C_x, is plotted against the phase for the two motion frequencies, as shown in Fig. 14. The upstroke (US) and downstroke (DS) periods are indicated at the top of the plot. For reference, the static drag coefficient at 90° angle of attack, $C_d = 0.95$ (Xu et al. 2025), is shown as a gray line. At the higher reduced frequency ($k = 0.38$), C_x ranges from 1.2 to 3.5, exceeding the static value throughout the cycle. In contrast, at the lower frequency ($k = 0.19$), C_x varies between 0.8 and 1.8, remaining closer to the static reference. The force fluctuation amplitude at $k = 0.38$ is more than twice that at $k = 0.19$, consistent with the increased flow unsteadiness observed in the corresponding velocity fields.

To better understand the origin of the force coefficients, the individual contributions in Eq. 4, namely the mean momentum convection (MC) term, the pressure (press) term, the time derivative (TD) term, and the turbulence momentum transfer (TMT) term, are shown in Fig. 15a and b for the two reduced frequency cases at each phase for the plunging motion. These terms are defined as:

$$\mathrm{MC} = -\rho \oint_C \bar{u}_i \bar{u}_j n_j \, \mathrm{d}l \tag{8}$$

$$\mathrm{press} = -\oint_C \bar{p} n_i \, \mathrm{d}l \tag{9}$$

$$\mathrm{TD} = -\rho \frac{\partial}{\partial t} \oint_C \bar{u}_i n_j x_j \, \mathrm{d}l \tag{10}$$

$$\mathrm{TMT} = -\rho \oint_C \overline{u_i' u_j'} n_j \, \mathrm{d}l \tag{11}$$

The mean viscous stress term is omitted due to its negligible magnitude. For the streamwise force contribution, the pressure term dominates the overall loading, while the MC term provides the second-largest contribution, varying in phase with the motion. In general, each force contribution is greater at $k = 0.38$ than at $k = 0.19$. For example, the maximum pressure contribution at $k = 0.38$ (occurring at $\phi = 90°$) exceeds the corresponding maximum at $k = 0.19$ (occurring at $\phi = 260°$) by more than 55%. This is related to the relative location between the vortex pair and the airfoil surface. For $k = 0.19$ case, the LEV and TEV pair is extended to more than $3c$ downstream (Fig. 9), while for the higher-frequency case, the vortex pair stays closer to the airfoil surface (on average stays within $3c$, see Fig. 13), which leads to higher pressure, and overall high C_x.

Figure 14 shows that for both frequencies, C_x peaks near the transition between upstroke and downstroke, which are near $\phi = 90°$ and 270°. At these two extreme plunging locations, the wake vortices are developed with relatively high

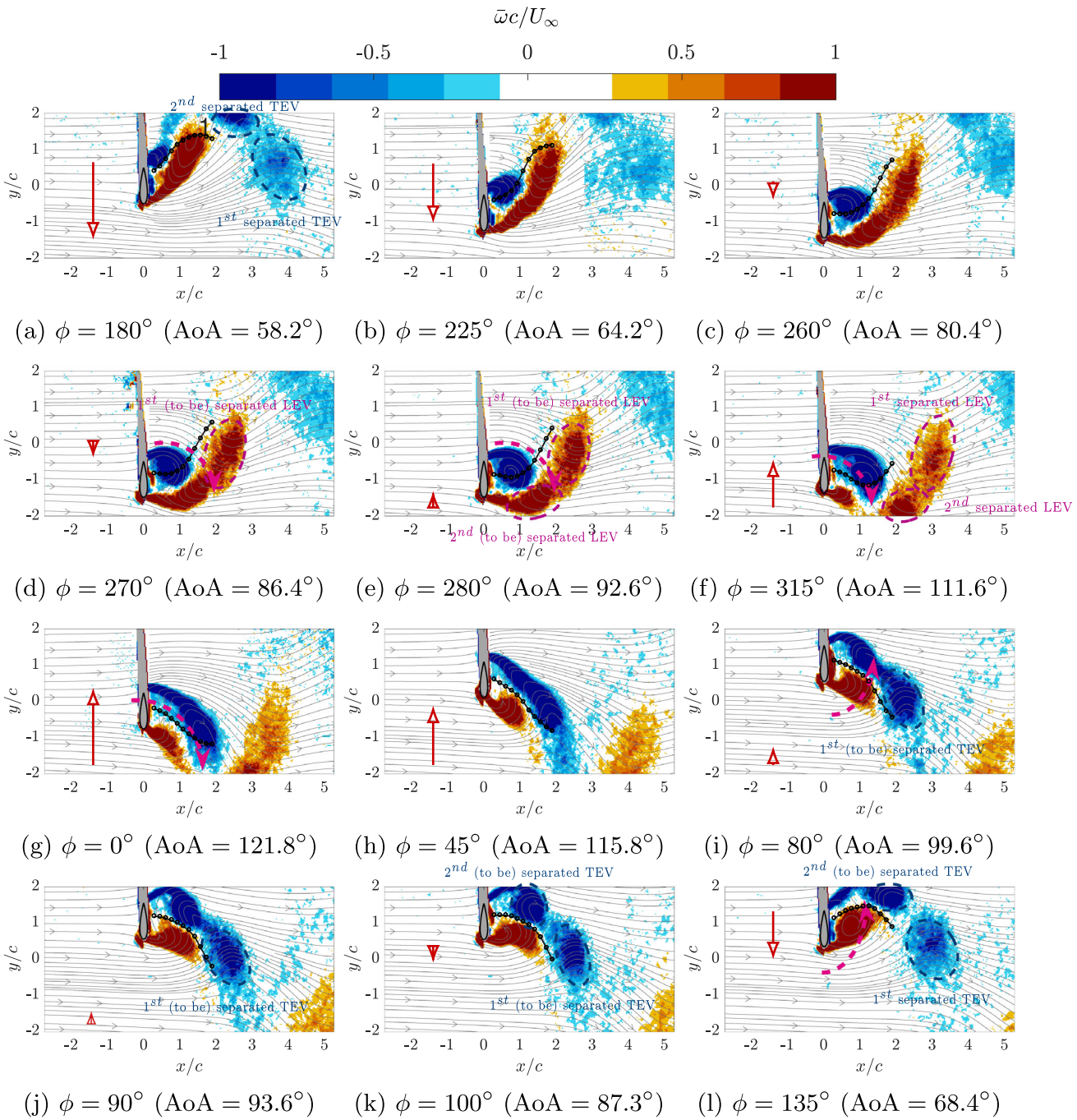

Fig. 13 Contours of the phase-averaged spanwise vorticity component superimposed with streamlines. Vortex identified using Γ_1 method for the $k = 0.38$ surging case. The red arrow represents the scaled motion velocity $\dot{h}$. The wake center line is marked by the black circled line

circulations. As shown in Fig. 10, near $\phi = 90°$, TEV develops the most, with the next phase being vortex separation. Meanwhile, at this phase, the LEV is also developed with a high vorticity and circulation ($\frac{\Gamma}{U_\infty c} = 1.9$ at $k = 0.38$ and 2.7 at $k = 0.19$). Similarly, at $\phi = 270°$, the LEV develops with a high circulation: at $k = 0.38$, $\frac{\Gamma}{U_\infty c} = 3.1$, and the separation of the rear part of the LEV happens shortly after ($\phi = 280°$); similarly at $k = 0.19$, $\frac{\Gamma}{U_\infty c} = 2.8$ at $\phi = 270°$. Overall, the developed vortex pairs near the transition between the upstroke and downstroke lead to the highest circulatory force on the airfoil, which is demonstrated as the force peaks as shown in Fig. 14.

Interestingly, at $k = 0.38$, C_x also presents a local minimum value of 1.2 at $\phi = 180°$. In contrast, the C_x distribution does not display a pronounced local minimum, but rather two comparable maxima at $\phi = 80°$ and $\phi = 260°$. The smallest

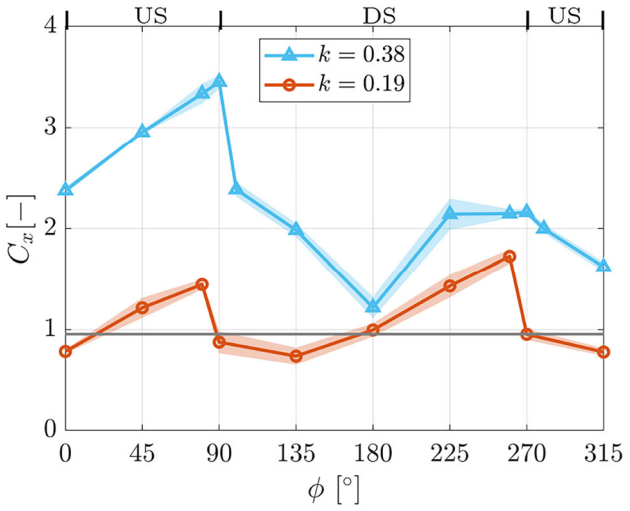

Fig. 14 (a) streamwise force coefficient C_x at each plunging phase for the two motion cases. The shaded area indicates the 95% confidence interval from different boundary tests. The US and DS period is marked on top of the figure. The solid gray line indicates the static drag coefficient at 90° angles of attack

value appears at $\phi = 135°$ ($C_x = 0.7$), yet it is not substantially lower than those in the adjacent phases. In order to compare the different performance at the two reduced frequencies, the pressure coefficient field C_p is plotted together for $\phi = 90°$ (the highest C_x at $k = 0.38$), $\phi = 180°$, and $\phi = 270°$ at $k = 0.38$, and $\phi = 80°$, $\phi = 135°$, and $\phi = 260°$ (the highest C_x at $k = 0.19$) at $k = 0.19$, as shown in Fig. 16.

As shown in the vorticity plots at $k = 0.38$ at $\phi = 90°$ (Fig. 13j) and $\phi = 180°$ (Fig. 13a), the TEV has just shed at $\phi = 180°$, whereas at $\phi = 90°$ the exhibited vortices contribute to lower circulation (higher magnitude), with the non-dimensionalized value decreasing from approximately -0.7 to -3 (illustrated in Fig. 10). Consequently, in the wake region, $\phi = 90°$ exhibits a much lower pressure coefficient (higher magnitude, as shown in Fig. 15), with a minimum of approximately -3, compared to $\phi = 180°$, where the negative C_p region is smaller with the minimum value near -1.8. For these two phases, the two most dominant force contributions (pressure term and MC) on the control boundary are shown in Fig. 17. The control contour presented here has a fixed 20 dx distance from each boundary of the airfoil surface. The curves start from the bottom left of the control contour, with the four sides marked as shown in Fig. 6. In the pressure contour plot (Fig. 17), although the front contour shows a similar pressure contribution at both phases, the back contour at $\phi = 90°$ exhibits significantly higher pressure contribution.

At $k = 0.38$, another noticeable difference is observed between the two extreme phases at $\phi = 90°$ (Fig. 16) and $\phi = 270°$ (Fig. 16). At $\phi = 90°$, two suction regions are located at the LEV and TEV in the wake, while at $\phi = 270°$, the suction is smaller and concentrated mainly at the TEV. To better

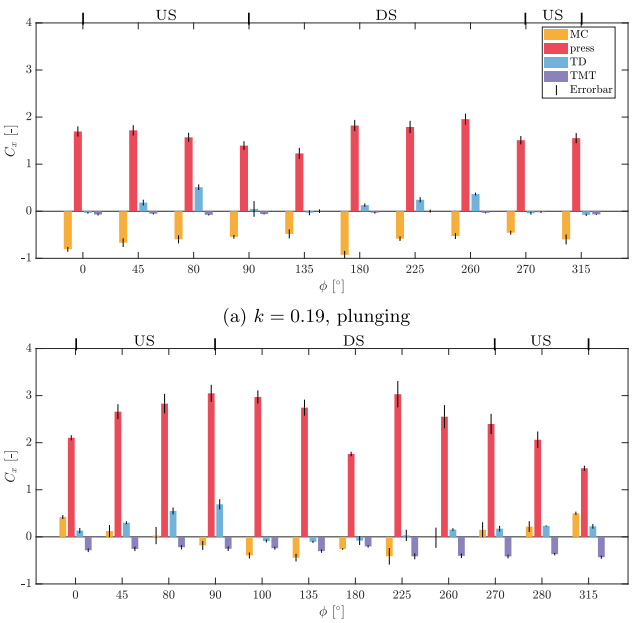

(a) $k = 0.19$, plunging

(b) $k = 0.38$, plunging

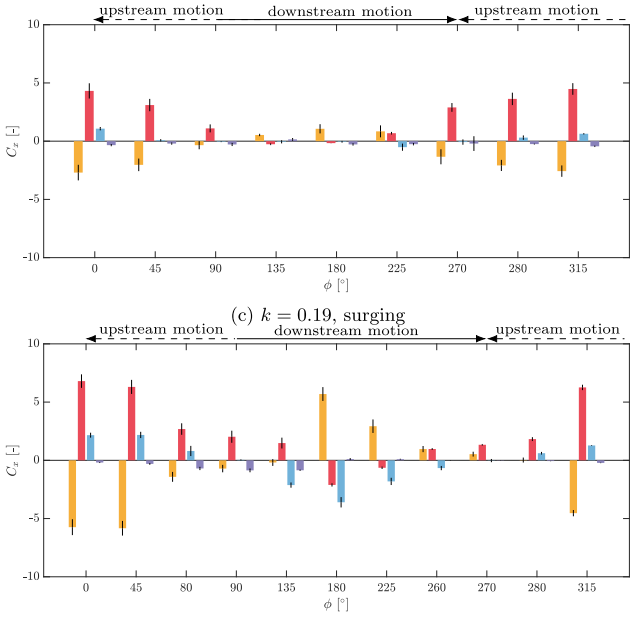

(c) $k = 0.19$, surging

(d) $k = 0.38$, surging

Fig. 15 Streamwise aerodynamic force contribution at $k = 0.19$ and $k = 0.38$ from mean convection (MC), pressure (press), turbulent momentum transfer (TMT), and time derivative (TD) for both the plunging and surging cases. The definitions of each term are shown from Equation 8 to Equation 11. The error bar height represents the 95% confidence intervals from different boundary tests

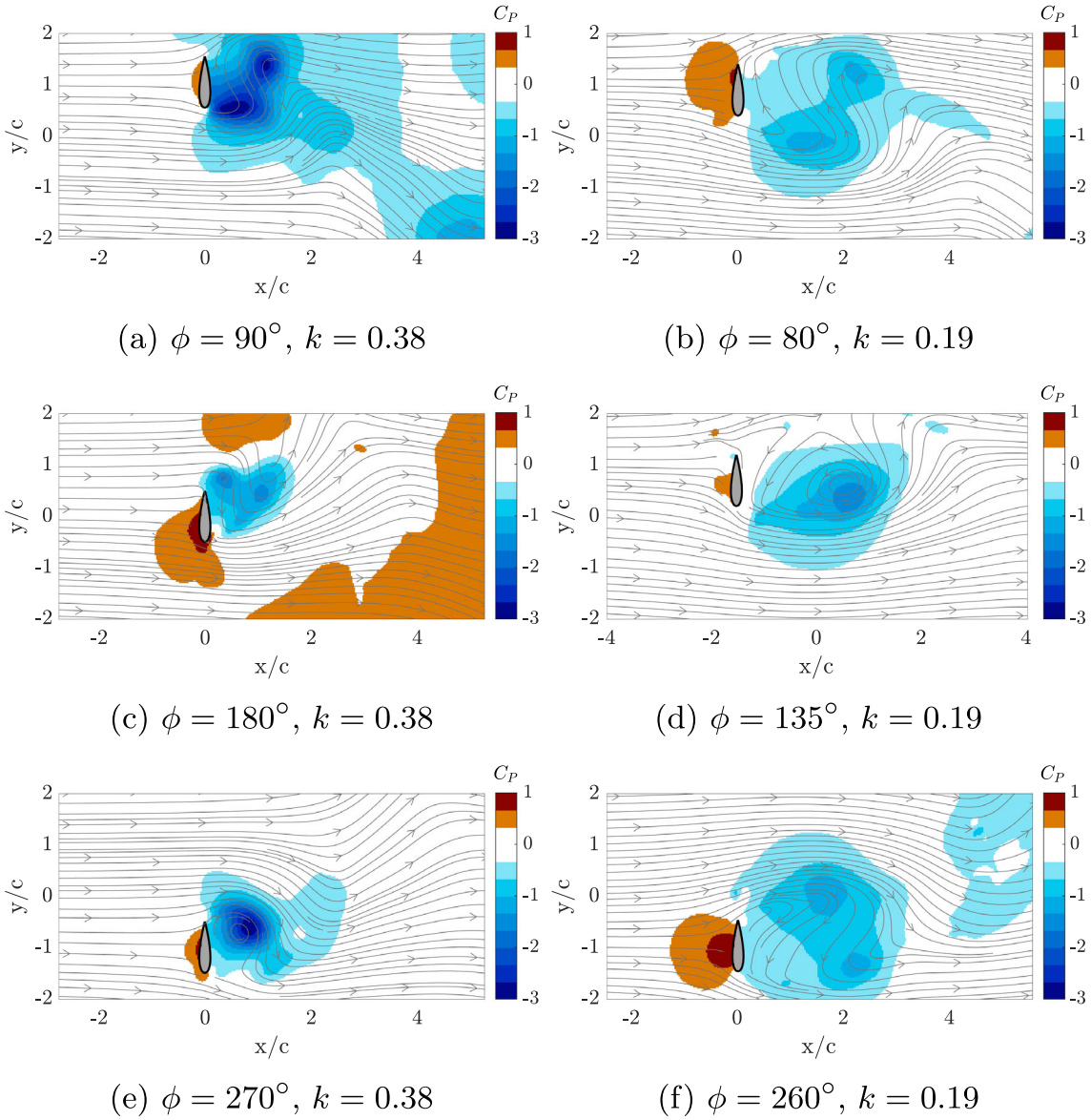

Fig. 16 Pressure field C_p at representative phases at the two reduced frequencies

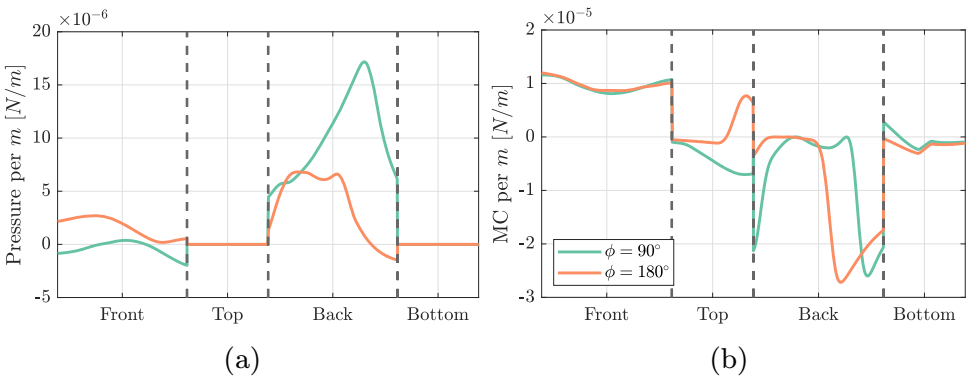

Fig. 17 (a) pressure term and (b) MC in the streamwise direction in Eq.4 for $\phi = 90°$ and $\phi = 180°$ at $k = 0.38$

understand the relationship between the vorticity field and the pressure, these two fields were analyzed with a higher C_p range between −4 and 4 (not shown). The analysis shows that the TEVs are well developed at both phases, each containing a fully reversed flow region. In contrast, the LEV exhibits a strong dependence on the instantaneous angle of attack: at $\phi = 90°$, the LEV vorticity is high ($\bar{\omega}c/U_\infty \geq 4$), whereas at $\phi = 270°$, it is weaker ($\bar{\omega}c/U_\infty \approx 2$). This demonstrates that at higher k, the high-frequency motion alters the shear layer evolution, leading to different vorticity flux and vortex roll-up between phases. This demonstrates that at high k, the large angle of attack variations amplify differences in vorticity and pressure distribution between phases.

However, at the lower reduced frequency ($k = 0.19$), the distinction between the highest C_x phase ($\phi = 260°$, peak C_x) and the lowest C_x phase ($\phi = 135°$) becomes less pronounced. This is evident in the pressure coefficient fields (Fig. 15f and d), which both show a similar high-pressure region on the upwind side and comparable low-pressure regions in the wake (with the minimum reaching approximately $C_p = -1.2$). The same trend can be observed between the two extreme phases at $\phi = 80°$ and $\phi = 260°$, where the wake contains two local suction regions associated with the LEV and TEV. At $\phi = 80°$, the suction is slightly stronger near the LEV, while at $\phi = 260°$ (Fig. 9) it shifts toward the TEV. In the meantime, the suction in the upwind side of the airfoil is higher at $\phi = 260°$ than at $\phi = 80°$. Overall, at low k, the smaller angle of attack variations result in a less varied flow topology and pressure distribution between different phases, producing smaller force variations compared to the high-k case.

The MC term, shown in Fig. 16, exhibits similar contributions at both phases at $k = 0.38$ along the front and bottom boundaries. The streamwise velocity plots (Fig. 11j and a) indicate that the incoming flow from the left, combined with the accelerated flow induced by the airfoil motion and the lower boundary layer, generates comparable flow dynamics in these regions. However, the difference between these two phases lies in the top and back control boundaries. As shown in the second term on the right-hand side of Equation4, the MC term is primarily governed by the product of streamwise and crossflow velocities. The crossflow velocity distributions $\bar{v}/U_\infty$ at these two phases are presented in Fig. 18, where the black rectangle denotes the force integration contour around the airfoil. At $\phi = 90°$, the airfoil reaches the end of the upstroke, and the wake retains upward inertia, producing positive $\bar{v}/U_\infty$ in the near wake. In contrast, during the downstroke at $\phi = 180°$, negative $\bar{v}/U_\infty$ develops in the wake. This phase-dependent difference in crossflow velocity accounts for the distinct MC contributions from the top and back boundaries. As a result, as shown in Fig. 18, the MC contribution at $\phi = 90°$ and $\phi = 180°$ presents opposite contributions.

Overall, due to the higher vorticity magnitude and the more horizontally oriented near wake, the streamwise force distribution at $\phi = 90°$ exhibits a much stronger pressure contribution together with a positive MC term. In contrast, at $\phi = 180°$, the pressure contribution is weaker and the MC term becomes negative as a result of the skewed wake. Consequently, when combined with the minor TD and TMT terms, $\phi = 90°$ corresponds to the maximum streamwise force within the cycle, whereas $\phi = 180°$ corresponds to the minimum.

The drag and lift coefficients, C_d and C_l, are plotted against ϕ in Fig. 19a, b, respectively. These coefficients are obtained from the effective angle of attack, together with the force coefficients C_x and C_y (crossflow force coefficient), using the relations $C_d = C_x \sin(\text{AoA}) + C_y \cos(\text{AoA})$ and $C_l = C_x \cos(\text{AoA}) - C_y \sin(\text{AoA})$. C_d is in the same direction as U_{rel} as shown in Fig. 4, and C_l is perpendicular to it. The static results reported by Holst et al. (2019) were interpolated based on the AoA at each phase for the two motion cases and are shown as dashed lines for comparison. Overall, with the static C_d varying between 0.68 and 0.88, the plunging motion produces substantially higher drag values in both cases. Similar to C_x, the peak C_d during the plunging cycle is approximately four times higher than the static case at $k = 0.38$ and more than twice as high at $k = 0.19$. The largest deviations between the plunging and static results occur when the acceleration is highest, near $\phi = 90°$ and $\phi = 270°$.

For the lift coefficient, C_l, the plunging motion generally follows the trend of the static case, particularly for $k = 0.19$. Between $\phi = 0°$ and 90°, and between $\phi = 270°$ and 315°, the angle of attack exceeds 90°, resulting in negative C_l, whereas between $\phi = 90°$ and 270°, AoA < 90° produces positive C_l. Especially at $k = 0.19$, the plunging C_l closely matches the static values. In contrast, at $k = 0.38$, the negative C_l regions exhibit much lower values (approximately −1.45) compared to the static case (approximately −0.3). In the positive C_l region, however, the overall trend remains similar, though with larger peaks around $\phi = 135°$ and $\phi = 225°$.

These results indicate that plunging motion fundamentally alters the aerodynamic forces relative to the static case. While C_l retains some resemblance to the static behavior, particularly at lower reduced frequency ($k = 0.19$), the increasing deviations at higher k highlight the importance of vortex dynamics and flow unsteadiness induced by motion with varying accelerations. In contrast, the consistently elevated C_d compared to the static cases demonstrates that plunging introduces substantial additional drag through unsteady vortex shedding, which cannot be captured by a static polar.

The coefficients C_d and C_l are also plotted against the angle of attack, forming hysteresis loops as shown in Fig. 19c, d. The static values from Holst et al. (2019) are indi-

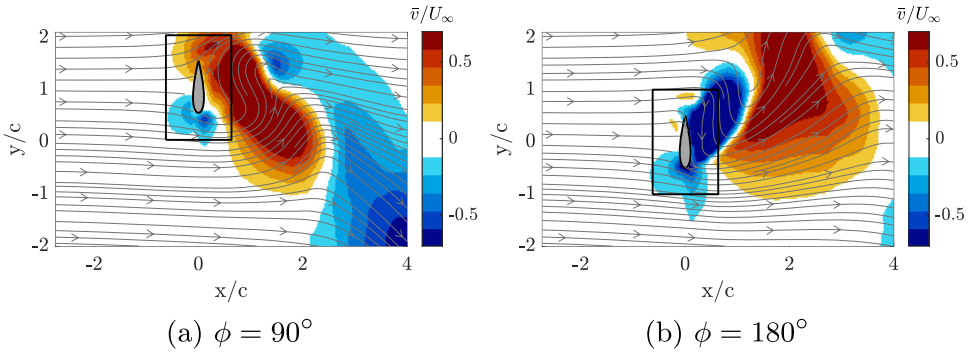

Fig. 18 Crossflow velocity $\bar{v}/U_\infty$ for (a) $\phi = 90°$ and (b) $\phi = 180°$ at $k = 0.38$. The black rectangle represents the force integration contour. Note that the shadow region on the top of the airfoil is interpolated for load integration purposes

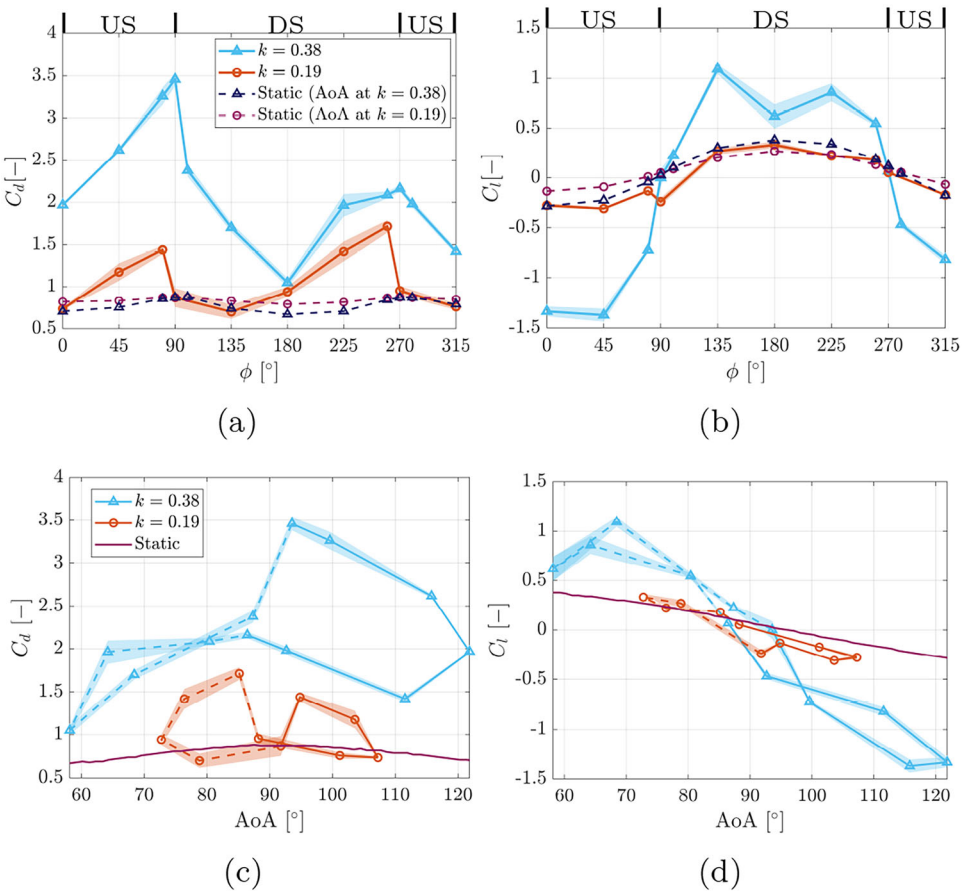

Fig. 19 Aerodynamic coefficients plotted with phase (**a**) and (**b**) and effective angle of attack (**c**) and (**d**). Note that the static results are interpolated from the wind tunnel measurement from Holst et al. (2019)

cated by the purple line in each plot. In the hysteresis plots, the solid line corresponds to the mean values during the upstroke period, while the dashed line represents those during the downstroke.

For both reduced frequency cases, the C_l hysteresis loops remain close to the static values, especially for the $k = 0.19$ case. At $k = 0.38$, the C_l values diverge from the static results outside the AoA close to 90° region. However, the variations between the increasing angle of attack phases and decreasing angle of attack phases are small, which is consistent with the inherent small lift values in this angle range.

In contrast, the C_d hysteresis loops show pronounced differences between the increasing and decreasing angle of attack phases. For $k = 0.38$, the strongest hysteresis occurs during the upstroke period, where AoA varies between 90° and 128° (corresponding to phases $\phi = 0°$–$90°$ and $\phi = 270°$–$315°$; see Fig. 5). This behavior arises because, at $k = 0.38$, the LEV and TEV grow and shed at different phases during the upstroke period: the LEV sheds between $\phi = 270°$ and 0° (Fig. 9d–g), while the TEV sheds between $\phi = 0°$ and 90° (Fig. 9g–j). The resulting strong variations in vorticity, circulation, and force lead to the pronounced C_d hysteresis during the upstroke. In contrast, during the downstroke ($\phi = 90°$–$270°$; see Figs. 9j–l and a–d), both the LEV and TEV continue to grow without shedding from the airfoil. As a result, the force variations are smaller, and the hystere-

sis in C_d is much weaker compared to the upstroke period. The presence of maximum hysteresis during the upstroke is consistent with the findings of Visbal (2011) and Miotto et al. (2022). Although their operating conditions ($k = 0.25$, maximum effective angle of 22°) resulted in a correspondingly lower maximum C_d of approximately 0.4, the fundamental asymmetry in the hysteresis loop closely mirrors the behavior observed in the present study.

However, for the low-frequency case at $k = 0.19$, the differences in magnitudes between the increasing and decreasing angle of attack phases are most evident near AoA = 85.2° (during downstroke, the peak on the dashed line) and 94.8° (during upstroke, the peak on the solid line), corresponding to the transition phases between upstroke and downstroke ($\phi = 260°$–$270°$ and $\phi = 80°$–$100°$ respectively), as shown in Fig. 5. Because the plunging acceleration reaches its maximum at these stroke reversal points, this result indicates that at lower reduced frequencies, where circulatory forces from the vortices are weaker, the hysteresis is primarily governed by non-circulatory effects from the added mass forces.

3.2.1 Comparison between the plunging motion and the surging motion

As mentioned in Sect. 2.1, the same parameter space, experimental setup (except for the motion orientation) was previously applied to the surging airfoil motion, where the airfoil is moving parallel with the wind under 90° angle of attack. In order to compare the difference due to different motion kinematics, the force terms listed from Eqs. 8 to 11 are computed with the same control boundary condition, explained in Sect. 2.5.1. The results are shown in Fig. 15.

Compared with the surging motion discussed in Xu et al. (2025), three main differences are observed in the overall force variations and individual force contributions:

- Overall force variation: In surging motion, the airfoil moves parallel to the incoming wind, so the angle of attack remains fixed at 90°. Due to the direct effect of the wind in the vertical direction, C_x (equaling C_d for the surging case) exhibits approximately 67% larger variations compared to the plunging case, which ranges from 0.8 to 3.5, as shown in Fig. 14. much larger variations, ranging from approximately −1.5 to 3 (Xu et al. 2025), compared to 0.8 to 3.5 for the plunging motion. In addition, because plunging involves variations in AoA, forces are generated outside the x direction, and C_l shows noticeable variations (between −1.3 and 1 at $k = 0.38$) despite the inherently small static values near AoA = 90°.
- Force contributions in the streamwise direction: The results for the selected control boundaries tests for the surging cases are shown in Fig. 15c and d. Overall, the result of the selected control boundaries for the surging case shows similar mean values and confidence intervals compared to the higher range results in Xu et al. (2025). Compared to surging, the variation of the pressure and MC terms in plunging is smaller within a cycle. For plunging, the pressure term ranges from 1.2 to 3.0 and the MC term from −0.9 to 0.4, accounting for both reduced frequency cases. By contrast, for surging (Fig. 14c and d), the variation at $k = 0.19$ is 0 to 5 for the pressure term and −3 to 0.5 for the MC term. At $k = 0.38$, the variation is even greater: approximately 50% higher for the pressure term and 130% higher for the MC term compared to the low-frequency case. This difference is attributed to the motion direction: in surging, the direct alignment with the incoming wind enhances pressure and MC variations, whereas in plunging, the varying AoA leads to a lower variation of the relative speed experienced by the airfoil, thus leading to lower variations of the individual load terms.
- Relative importance of MC and pressure terms: In plunging, the MC term is much smaller than the pressure term, whereas in surging, both are comparable in magnitude. This is because, in surging, the horizontal motion at a constant 90° angle of attack generates vortex shedding with a symmetric, fully reversed pattern (Xu et al. 2025). The wake, therefore, extends into a larger region of strong reverse flow ($\bar{u}/U_\infty < -0.5$), where significant velocity gradients produce strong momentum convection. As a result, the MC term becomes comparable to the pressure gradient term, and both contribute substantially to the local momentum balance. In contrast, plunging involves predominantly crossflow motion. The vertical acceleration of the airfoil induces large instantaneous pressure gradients that dominate the momentum balance, while the wake is shorter and less sustained. The reverse flow region is smaller and weaker (Figs. 7 and 11), leading to reduced momentum convection. Meanwhile, the shorter wake requires momentum to be restored over a smaller distance, which leads to larger pressure gradients and higher pressure magnitudes near the airfoil. Consequently, the pressure term dominates the momentum balance in plunging, whereas in surging, both the convective and pressure terms contribute comparably.

Overall, these differences show that, under the same motion amplitude, frequency, and incoming wind speed, the surging motion produces larger streamwise force variations, strongly influenced by the competing contributions of the pressure and MC terms. By contrast, in plunging, the streamwise force coefficient is dominated by pressure variations, and additional force is generated due to the crossflow motion.

4 Conclusion

In this study, the plunging motion of an airfoil has been experimentally investigated with emphasis on vortex dynamics, frequency lock-in, and intra-cycle aerodynamic force variations. To enable direct comparison with the surging motion presented in Xu et al. (2025), identical incoming flow conditions, motion amplitudes, and frequencies were used, and the angle of attack was fixed at 90°.

Phase-locked PIV measurements captured the flow fields at 12 phases for two reduced frequencies, $k = 0.19$ and $k = 0.38$. At the lower reduced frequency ($k = 0.19$), the rear part of one LEV–TEV pair was separated and convected downstream during the downstroke, while an additional LEV was generated during the upstroke. In this regime, the TEV dissipated into the wake rather than causing separation near the rear of the airfoil, thereby preventing the vortex shedding frequency from synchronizing with the motion frequency. Thus, unlike the surging case, lock-in did not occur. This difference arises because surging only changes the effective flow speed (with AoA = 90° constant), promoting synchronization, whereas plunging continuously alters the effective angle of attack, introducing asymmetry that generates extra vortical structures and disrupts lock-in.

At the higher reduced frequency ($k = 0.38$), two rear parts of the LEV–TEV pair were separated and convected into the downstream wake each cycle, with one pair formed by the interaction with the counter vortex. This result leads to frequency lock-in. However, the wake at this condition was shorter and contained a lower circulation magnitude compared to $k = 0.19$, due to the broader variation of the effective angle of attack. Comparing plunging with surging at this reduced frequency reveals that, while both motions exhibit frequency lock-in, their distinct kinematics produce fundamentally different shedding patterns. The crossflow motion requires a higher motion frequency to overcome asymmetric shedding vortices, highlighting that lock-in depends on both frequency and motion kinematics.

The aerodynamic load analysis further shows that the maximum streamwise force occurs during transitions between upstroke and downstroke, reaching $C_x \approx 3.5$ at $k = 0.38$, which is almost four times higher than the static value at $\alpha = 90°$ (Xu et al. 2025). Relative to the static measurement data from Holst et al. (2019), the plunging motion yields substantially higher C_d, especially near $\phi = 90°$ and 270°, where values are up to four times larger. For C_l, plunging at $k = 0.19$ closely follows the static case, but at $k = 0.38$ the increased unsteadiness produces higher C_l.

Finally, comparing the load estimation results with surging motion highlights three main distinctions. First, plunging produces smaller streamwise force variations within a cycle, with contributions dominated by pressure, whereas in surging, both pressure and mean convection terms play comparable roles. Second, plunging wakes are less sustained, producing weaker reverse flow regions in the wake, while surging wakes are more symmetric and show higher reverse flow magnitudes. Third, the different motion kinematics fundamentally alter the vortex dynamics and therefore the balance of force contributions. Under identical flow conditions and airfoil kinematics (frequency and amplitude of motion), surging motion generates larger and more balanced force variations, while plunging motion is primarily pressure-driven with reduced overall force variation but enhanced sensitivity to unsteady vortex dynamics.

The present work, based on phase-locked PIV, provides a fundamental understanding of vortex dynamics and the lock-in effect of plunging airfoils and their comparison with the surging cases. Future studies should aim for time-resolved measurements to obtain more detailed vortex information to characterize the airfoil wake dynamics.

Appendix: the reliability of the plunging motion

In order to ensure the data reliability of the presented phase-locked PIV, the airfoil location at each phase was constantly checked throughout the wind tunnel test. To quantify the motion reliability, in Fig. 20 we present the location of the airfoil trailing edge on each measured image (200 in total for each phase) under the high-reduced-frequency case ($k = 0.38$), from the most upstroke ($\phi = 90°$) and most downstroke ($\phi = 270°$) position.

At these two extreme locations, the standard deviation (σ) remains minimum, which is 9×10^{-5} m and 0.002 m for the most upstroke and most downstroke, respectively. This low level of variance demonstrates that the motion is highly repeatable and robust.

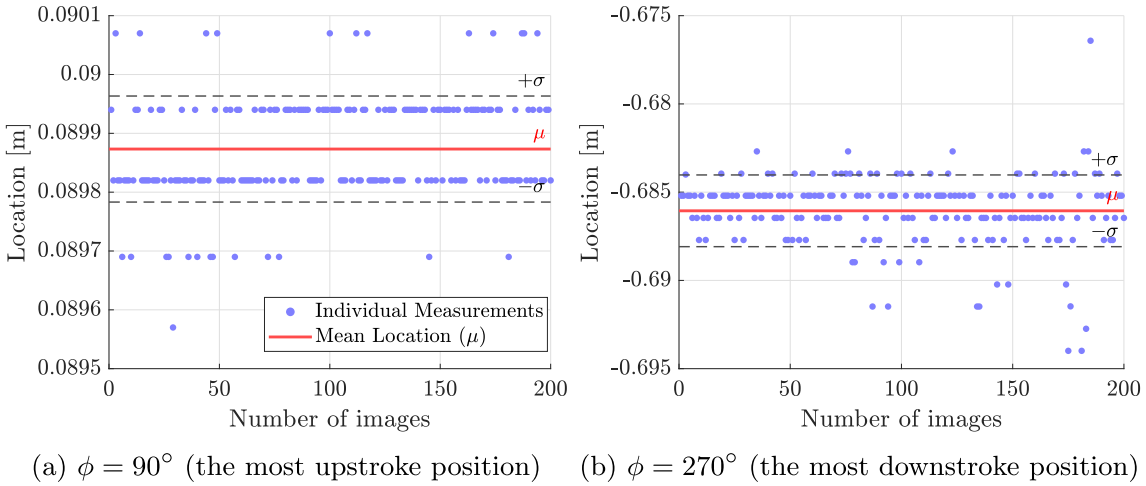

(a) $\phi = 90^\circ$ (the most upstroke position) (b) $\phi = 270^\circ$ (the most downstroke position)

Fig. 20 Location of the leading edge at the most upstroke and most downstroke position at the high frequency ($k = 0.38$) case

Acknowledgements We would like to express our gratitude to technicians Frits Donker Duyvis and Dennis Bruikman, as well as Kushal Kempaiah, for their invaluable assistance in preparing the wind tunnel campaign. We also thank Sowmya Iyer and the PhD researchers from the Wind Energy Section for their support and help during the campaign.

Author Contributions GX contributed to data curation, formal analysis, investigation, methodology, and writing—original draft. AS and CF contributed to conceptualization, formal analysis, methodology, supervision, and writing—reviewing and editing. WY contributed to conceptualization, formal analysis, funding acquisition, methodology, supervision, and writing—reviewing and editing.

Funding Not applicable.

Data Availability The available data can be found on 4TU.ResearchData with DOI: 10.4121/97b8ec78-c00c-4676-844b-84c8022c529f.

Declarations

Conflict of interest The authors declare no conflict of interest.

Ethics approval and consent to participate Not applicable.

Consent for publication The authors consent for publication.

Materials availability Not applicable.

References

Ajay AG, Ferreira CS (2024) A numerical investigation of wake recovery for an H- and X-shaped vertical-axis wind turbine with wake control strategies. Phys Fluids. https://doi.org/10.1063/5.0244810

Anagnostopoulos P (2000) Numerical study of the flow past a cylinder excited transversely to the incident stream. Part 1: Lock-in zone, hydrodynamic forces and wake geometry. J Fluids Struct 14:819–851. https://doi.org/10.1006/jfls.2000.0302

Benner BM, Carlson DW, Seyed-Aghazadeh B, Modarres-Sadeghi Y (2019) Vortex-induced vibration of symmetric airfoils used in vertical-axis wind turbines. J Fluids Struct 91:102577. https://doi.org/10.1016/J.JFLUIDSTRUCTS.2019.01.018

Bearman PW (1984) Vortex shedding from oscillating bluff bodies. Ann Rev Fluid Mech 16:195–222

Bishop RED, Hassan AY (1964) The lift and drag forces on a circular cylinder oscillating in a flowing fluid. Proc R Soc Lond Seri A Math Phys Sci 277(1368):51–75

Besem FM, Kamrass JD, Thomas JP, Tang D, Kielb RE (2016) Vortex-induced vibration and frequency lock-in of an airfoil at high angles of attack. J Fluids Eng Trans ASME. https://doi.org/10.1115/1.4031134

Bensason D, Mulay J, Sciacchitano A, Ferreira C (2025) Experimental demonstration of regenerative wind farming using a high-density layout of vertical-axis wind turbines. Wind Energy Sci 10(7):1499–1528. https://doi.org/10.5194/wes-10-1499-2025

Choi J, Colonius T, Williams DR (2015) Surging and plunging oscillations of an airfoil at low Reynolds number. J Fluid Mech 763:237–253. https://doi.org/10.1017/jfm.2014.674

Govardhan R, Williamson CHK (2000) Modes of vortex formation and frequency response of a freely vibrating cylinder. J Fluid Mech 420:85–130. https://doi.org/10.1017/S0022112000001233

GWEC: Global wind report 2024. Technical report, Brussels (2024) www.gwec.net

Holst D, Balduzzi F, Bianchini A, Church B, Wegner F, Pechlivanoglou G, Ferrari L, Ferrara G, Nayeri CN, Paschereit CO (2019) Static and dynamic analysis of a NACA 0021 airfoil section at low Reynolds numbers based on experiments and computational fluid dynamics. J Eng Gas Turbines Power 141(5):51015–51016. https://doi.org/10.1115/1.4041150

Horcas SG, Barlas T, Zahle F, Sørensen NN (2020) Vortex induced vibrations of wind turbine blades: influence of the tip geometry. Phys Fluids 32(6):065104. https://doi.org/10.1063/5.0004005

Horcas SG, Madsen MHA, Sørensen NN, Zahle F (2018) Suppresing vortex induced vibrations of wind turbine blades with flaps. in: the 7th European Conference on Computational Fluid Dynamics (ECFD 7) European Community on Computational Methods in Applied Sciences. https://doi.org/10.1007/978-3-030-11887-7_2

Horcas SG, Sørensen NN, Zahle F, Sørensen NN, Pirrung GR, Barlas T (2022) Vibrations of wind turbine blades in standstill: mapping the influence of the inflow angles. Phys Fluids 34:54105. https://doi.org/10.1063/5.0088036

Hu P, Sun C, Zhu X, Du Z (2021) Investigations on vortex-induced vibration of a wind turbine airfoil at a high angle of attack via modal analysis. J Renew Sustain Energy 13(3):033306. https://doi.org/10.1063/5.0040509

Heinz JC, Sørensen NN, Zahle F, Skrzypiński W (2016) Vortex-induced vibrations on a modern wind turbine blade. Wind Energy 19(11):2041–2051. https://doi.org/10.1002/WE.1967

Koopmann GH (1967) The vortex wakes of vibrating cylinders at low Reynolds numbers. J Fluid Mech 28(3):501–512. https://doi.org/10.1017/S0022112067002253

Leishman GJ (2006) Principles of helicopter aerodynamics. Cambridge University Press, Cambridge

Lin CT, Tsai ML, Tsai HC (2023) Flow control of a plunging cylinder based on resolvent analysis. J Fluid Mech. https://doi.org/10.1017/jfm.2023.526

Meneghini JR, Bearman PW (1995) Numerical simulation of high amplitude oscillatory flow about a circular cylinder. J Fluids Struct 9(4):435–455

Meskell C, Pellegrino A (2019) Vortex shedding lock-in due to pitching oscillation of a wind turbine blade section at high angles of attack. Int J Aerosp Eng. https://doi.org/10.1155/2019/6919505

Miotto R, Wolf W, Gaitonde D, Visbal M (2022) Analysis of the onset and evolution of a dynamic stall vortex on a periodic plunging aerofoil. J Fluid Mech. https://doi.org/10.1017/jfm.2022.165

Pirrung GR, Grinderslev C, Sørensen NN, Riva R (2024) Vortex-induced vibrations of wind turbines: from single blade to full rotor simulations. Renew Energy 226:960–1481. https://doi.org/10.1016/j.renene.2024.120381

Rival DE (2017) Oudheusden Bv (2017) Load-estimation techniques for unsteady incompressible flows. Exp Fluids 58(3):1. https://doi.org/10.1007/s00348-017-2304-3

Ragni D, Van Oudheusden BW, Scarano F (2011) Non-intrusive aerodynamic loads analysis of an aircraft propeller blade. Exp Fluids 51(2):361–371. https://doi.org/10.1007/S00348-011-1057-7/FIGURES/11

Sarpkaya T (2004) A critical review of the intrinsic nature of vortex-induced vibrations. J Fluids Struct 19(4):389–447. https://doi.org/10.1016/j.jfluidstructs.2004.02.005

Skrzypiński W, Gaunaa M, Heinz J (2016) Modelling of vortex-induced loading on a single-blade installation setup. J Phys: Conf Ser. https://doi.org/10.1088/1742-6596/753/8/082037

Shirzadeh R, Weijtjens W, Guillaume P, Devriendt C (2015) The dynamics of an offshore wind turbine in parked conditions: a comparison between simulations and measurements. Wind Energy 18(10):1685–1702. https://doi.org/10.1002/we.1781

Meerendonk R, Perçin M, Van Oudheusden, B (2016) Three-dimensional flow and load characteristics of flexible revolving wings at low Reynolds number. In: 18th international symposium on the application of laser and imaging techniques to fluid mechanics: Lisbon, Portugal

Visbal MR (2011) Numerical investigation of deep dynamic stall of a plunging airfoil. AIAA J 49(10):2152–2170. https://doi.org/10.2514/1.J050892

Van Oudheusden BW (2016) PIV-based pressure measurement. Meas Sci Technol 24:32. https://doi.org/10.1088/0957-0233/24/3/032001

Williamson CHK, Govardhan R (2004) Vortex-induced vibrations. Ann Rev Fluid Mech 36:413–455. https://doi.org/10.1146/annurev.fluid.36.050802.122128

Williamson CHK, Roshko A (1988) Vortex formation in the wake of an oscillating cylinder. J Fluids Struct 2:355–381

Xu G, Sciacchitano A, Ferreira C, Yu W (2025) On the unsteady aerodynamics of a surging airfoil at 90° incidence. Exp Fluids 66(5):85. https://doi.org/10.1007/s00348-025-04011-2

Zou F, Riziotis VA, Voutsinas SG, Wang J (2015) Analysis of vortex-induced and stall-induced vibrations at standstill conditions using a free wake aerodynamic code. Wind Energy 18(12):2145–2169. https://doi.org/10.1002/WE.1811